Density Functional Theory Techniques for Electron Energy Loss Analysis of Lithium Materials

Quentin Stoyel, Mining and Materials Engineering, McGill University, Montreal

Month and Day of submission

A thesis submitted to McGill University in partial fulfillment of the requirements of the degree of Masters of Science

Abstract

A new method of calculating the magnitude of the core hole screening in the case of lithium materials is developed and implemented for the accurate simulation of Energy Loss Near Edge Structure (ELNES) taken at 30keV. ELNES is calculated for Li, Li_2O, and LiF with marked improvements in agreement between calculation and experiment, as well as superior quantitative and predictive abilities. The technique uses linear response theory to relate the electron density to the core hole shielding contribution from the valence electrons in a molecule. This contribution is then implemented via a non integer core hole in final state rule calculations.

Abstract in French too

Acknowledgements

To all those useful folks

Contribution to Original Knowledge

A new method of simulating ELNES with a focus on Lithium materials was developed. Density functional theory results are used to simulate Electron energy loss fine structure.

Contents

Chapter 1

Introduction

The study of lithium materials has become increasingly relevant in recent years [1]. In particular, the field has been driven by the need to develop improved and more cost effective battery materials [1]. This drive has come largely in part from increasing demands for electric vehicles and portable electrical devices demanding longer lifetimes and faster charging. All aspects of lithium ion batteries are currently being improved yet theoretical limits have not yet been achieved in an array of properties including capacity, charge density, and charge/discharge rates . In addition to performance, safety and the ability to reuse or recycle battery materials are also growing regions of study [2–4].

In the realm of performance, lithium ion batteries offer a wide range of advantages. Lithium is the third element on the periodic table and is lightweight with a very high charge densities. This allows for batteries to be smaller and lighter without sacrificing lifetime. Additionally, lithium's lightweight nature and small ion size make it highly mobile, which leads to superior discharge rates. Finally, as an alkali earth metal with a single weakly bound valence electron, lithium is highly electropositive allowing lithium ion batteries to achieve higher operating voltages than alternatives such as nickle-cadmium or lead-acid batteries [5]. These comparative performance advantages to these alternatives are illustrated in Fig 1.1 [5].

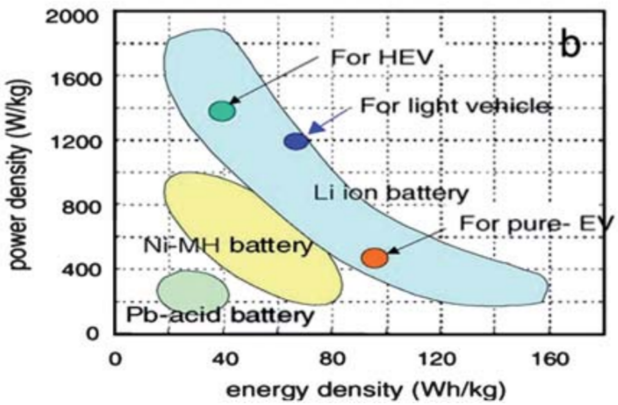

Figure 1.1: Plot illustrating the the power and energy densities achievable by three types of battery, as well as the minimum requirements for various types of electric vehicle, including hybrid electric vehicles (HEV), plug in hybrids (light vehicle). From [5]

The pursuit of developing new and improved battery materials has shifted analysis increasingly towards studying the microstructure of materials [6–8]. The ability to identify crystal structure, diffusion mechanics, and composition has become an essential element to understanding and tailoring material properties [9]. On this front, electron microscopy has become a central technique to this effort [10; 11]. Rapidly improving technology, the possibility of atomic level resolution, coupled with the increasing accessibility have made electron microscopy one of the most prevalent techniques for studying nanoscale features in materials [12]. Here, however lithium is at odds with the method. Novel battery materials are increasingly intricate and lithium's lightness and ionizable nature make it particularly sensitive to electron beams, and often require indirect analysis [13]. These properties make electron energy loss spectroscopy (EELS), a low dosage technique that is well suited for light elements such as lithium, attractive for battery material analysis [14]. Recent advances extending EELS into low voltage STEM have made EELS appropriate for a range of new materials [15]. However, EELS results are largely qualitative and unstudied systems require a degree of theoretical support. The theoretical support is all the more essential in dealing with novel technique of low voltage EELS required to study fragile lithium materials.

Theoretical support for EELS can come from a number of methods. The most prevalent of these are based in density functional theory (DFT), a first principles approach that requires only the locations of atoms in a crystal to determine material properties [16–20]. However, results have been limited to qualitative findings, and lithium's lightweight nature further complicates theoretical approaches [21; 22]. Much of the challenge in simulating EELS for lithium lies in the treatment of the electron hole created in excited atoms. Lithium's few core electrons mean that excitonic effects from the hole will always be present in the spectra. Current methods in literature lack the subtlety to treat these effects.

The goal of this work is to calculate meaningful EELS spectra of lithium materials, specifically in the unprecedented context of EELS at 30 keV. To achieve this goal, the focus is on improving the treatment of core electron holes of lithium in DFT simulations.

The outline of this thesis is as follows: in Chapter 2 presents an overview of EELS, DFT and theoretical EELS calculations. Chapter 3 describes the improved method developed in this work, and Chapter 4 applies the method to a number of lithium materials. Chapter 5 concludes the results and addresses future work.

Chapter 2

Literature Review

The focus of this work lies in first principle theoretical calculations of EELS calculations, designed to be performed without any experimental input. However, new theoretical techniques must be validated through comparison to experiment. To this end, this chapter commences with an overview of experimental electron microscopy and energy loss spectroscopy (EELS) before discussing the basis of first principles calculations, in this case density functional theory (DFT). The chapter concludes with a review of the various methods used to calculate EELS theoretically from DFT. The particularities of lithium materials will be discussed at each step of this process.

2.1 Electron Energy Loss Spectroscopy

2.1.1 Electron Microscopy

The drive to improve increasingly refined battery materials relies on characterizing the nano scale features which define their properties [23]. At these length scales, even state of the art light microscopes lack the resolution to discern these features [24]. This limitation is due to the fact that nano scale features fall well below the diffraction limit of light microscopes, given by [25]:

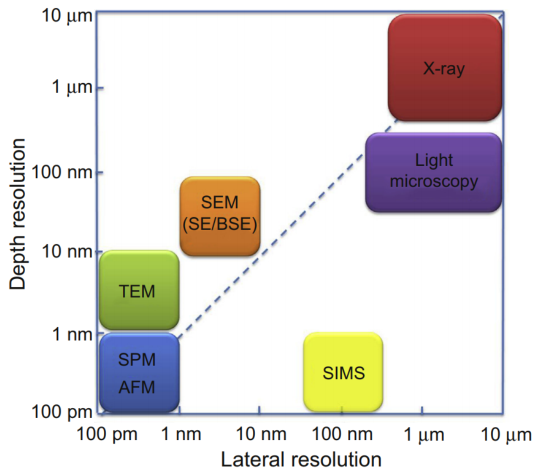

Figure 2.1: Resolution achievable by various techniques including Transmission and Scanning electron microscopy (TEM/SEM) and light microscopy, on a log-log scale. Taken from Inkson, 2016 [11]

.

$$d = \frac{\lambda}{2n\,\sin(\theta)} \tag{2.1}$$

Where n is the refractive index and d is the smallest distance between two discernible objects. For optical light (λ = 400-800nm), it is impossible to routinely achieve the desired resolution ($\sim$ 1-50 nm) for characterization [24]. Electrons however, have a wavelength dictated by [23]:

$$\lambda = \frac{h}{\sqrt{2m_0 eE}} \tag{2.2}$$

Where h is planck's constant, m_0, e and E are the rest mass, charge and energy of an electron. In an electron microscope, electrons are accelerated to energies in the order of 1-100 keV giving them wavelengths in the range from 1-100 pm (1pm = 10^{-12}m), far smaller than the distances between atoms ($\sim$0.5 nm) [26]. Electron microscopes can therefore achieve a far lower theoretical diffraction limit and are in fact currently limited by the technological constraints of the electron lenses [23]. This high resolution has made electron microscopy a key part of investigating material microstructure and is compared to other methods in Fig 2.1 [11].

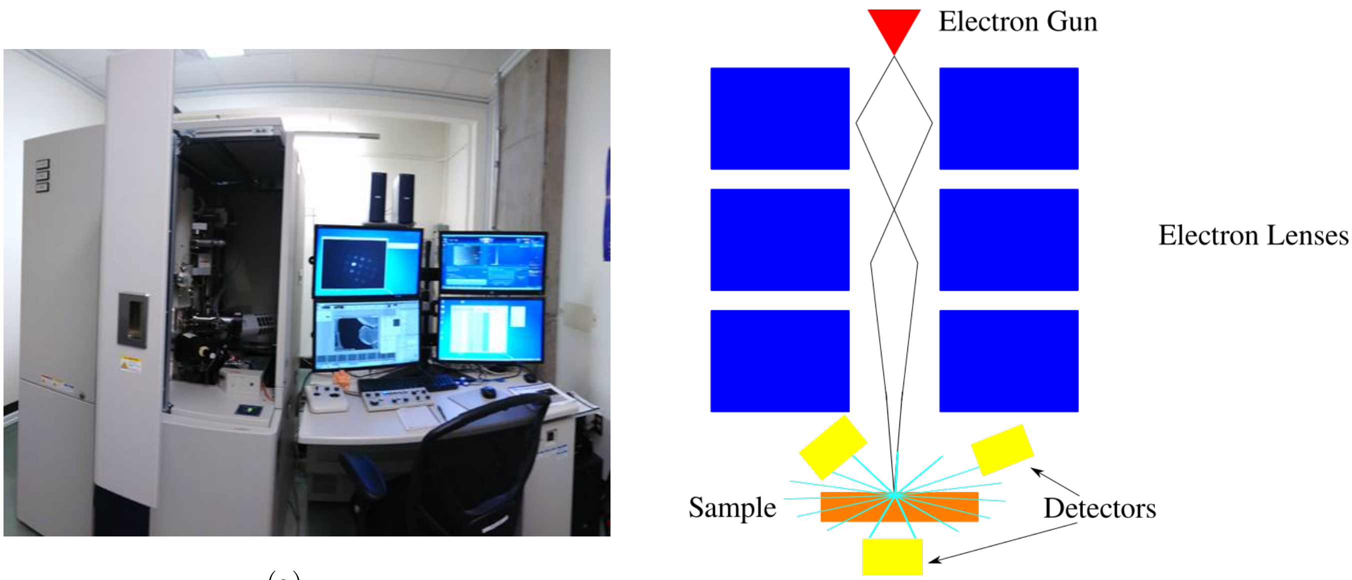

(a)

(b)

Figure 2.2: Example of an electron microscope (a) and working principles behind data acquisition (b).

In order to use obtain images using electrons, electron microscopes use magnetic lenes to direct a highly focused beam of high energy electrons onto a sample, and collect the assorted types of signal resulting from the interaction, see Fig 2.2.

The large number of different signals generated when the electron beam interacts with the sample, (Fig 2.3), can be used to perform a multitude of types of analysis [27]. The wide range of material properties that can be obtained at high spatial resolution make electron microscopy a very versatile technique. A full discussion of the analysis methods at the disposal of electron microscopes is beyond the scope of this work and has been well documented elsewhere [14; 23; 27; 28]. Instead, we will focus on the relevant technique, electron energy loss spectroscopy (EELS). EELS is an electron microscopy technique that analyzes the transmitted inelastically scattered electrons, Fig 2.3[14]. It is mainly an analytic technique, however it is also possible to perform imaging with EELS [29]. EELS consists of collecting electrons that have passed entirely through the sample and binning them according to how much energy each one has lost, resulting in a spectrum such as in Fig 2.4. The numerous

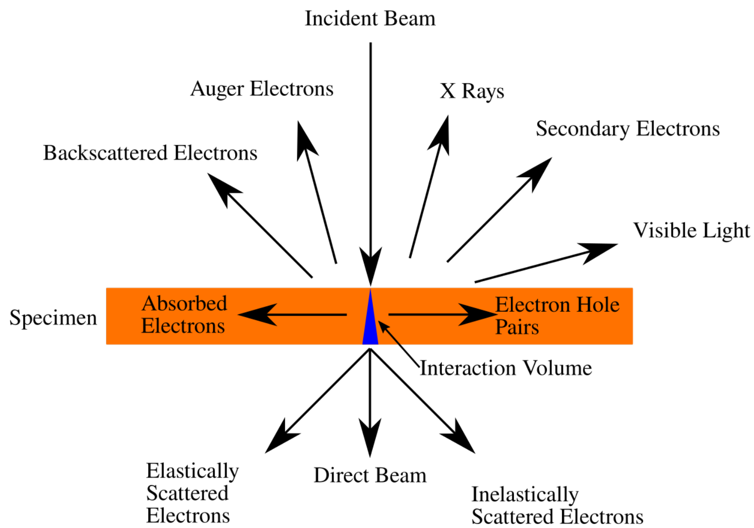

Figure 2.3: The numerous types of signals emitted when an electron beam encounters a sample in an electron microscope. Redrawn from Williams and Carter [27].

distinct features arise from the various mechanisms through which beam electrons can lose energy in the sample. Each mechanism results in a particular feature in the spectrum, of which the main ones are described below:

- **Zero Loss Peak (ZLP):** The majority of the electrons in EELS pass through the specimen without experiencing an inelastic interaction, and retain their initial energy. The width of the ZLP defines the resolution of the spectrum and is due to energy spreading as the beam passes through the electron lenses [30]. For thin samples, the ZLP is also the most intense feature on a spectrum [14].

- **Background:** Beam electrons can excite loosely bound electrons close to the Fermi level into the unoccupied conduction band. Due to the large number of possible transitions and the fact that high energy events are less favourable, this results in a smoothly decaying background [14].

- **Plasmon Peak:** The electron beam can excite multiple atoms in a solid collectively, creating a wavelike oscillation in the electron cloud of the solid [14]. These are called plasmon excitations and result in a peak appearing between 5eV-30eV [14]. The shape

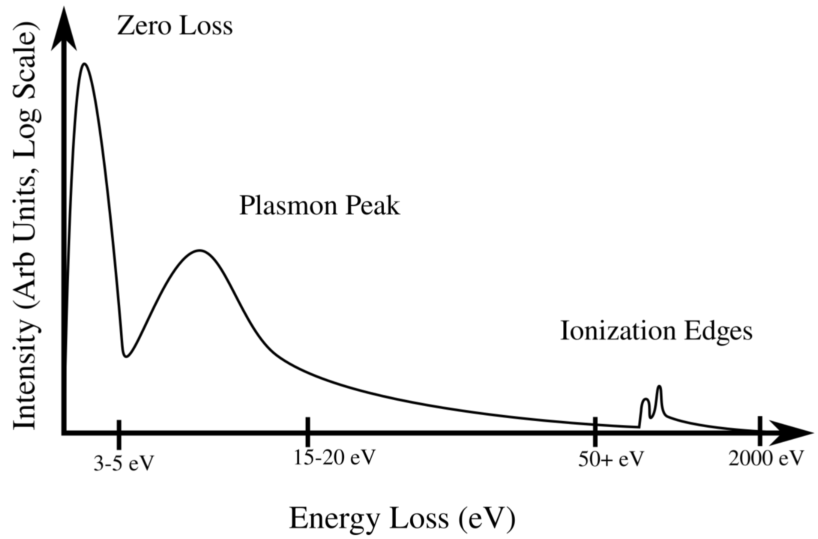

Figure 2.4: Sample EELS spectra identifying the main features, the zero loss peak, plasmon peak and ionization edges with fine structure. The intensities are on a log scale, and span approximately 6 orders of magnitude between the zero loss and the ionization edges.

and intensity of the plasmon peak is dependent on the bond strength of the material and can be used to probe properties such as thickness and surface topology [31; 32].

- **Ionization Edges:** Beam electrons can excite core electrons in a sample to the conduction band. As an atom's core states are in general, isolated from its surroundings, the "edges" for each element will occur at specific energy locations, independent of sample, analogous to characteristic x-rays [14]. These can be used to determine sample composition [14].

The array of independent interaction mechanisms opens the possibility of beam electrons undergoing multiple inelastic events in the sample, referred to as plural scattering. In order for meaningful data to be extracted from a spectra, plural scattering must be minimized [14]. This is achieved by using samples thinner or at least comparable to the path length of the beam electrons [14]. Thicker samples result in duplicate plasmon peaks which drown out the relatively weaker ionization edges see Fig 2.5. Consequently, samples must be made thin enough to analyze the more sensitive parts of EELS spectra, amongst others near edge

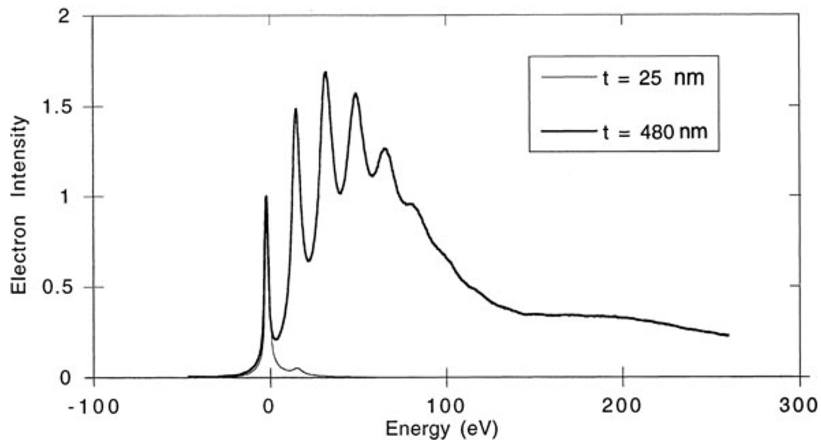

Figure 2.5: Two spectra demonstrating the importance of thin samples and single scattering events. In the thicker sample, plural scattering results in multiple evenly spaced plasmon peaks with intensities larger than the zero loss extending well past 100eV. The high background from the plasmon peaks and the thicker sample drown out any structure due to ionization edges [14]. Taken from Egerton, 2011 [14]

structure.

Near Edge Structure

Unlike x-ray edges in EDS which have distinct, simple shapes, the higher energy resolution in EELS reveals features in the ionization edges extending up 50 eV beyond the onset of the edge, referred to as energy loss near edge structure (ELNES) [14]. These features are a reflection of the unoccupied states in the conduction band that represent the final states available to sample electrons. The band structure of the conduction band is largely dependent on the local bonds of the atom in question. Because of this, ELNES can be used to investigate properties dependent on the local environment of each element. Crystal structure is one such property, and ELNES can be used to distinguish different crystal structures of the same element such as carbon in graphite vs diamond, see Fig 2.6 [33]. ELNES is also sensitive to impurities or dopants that would effect the band structure [34]. The large

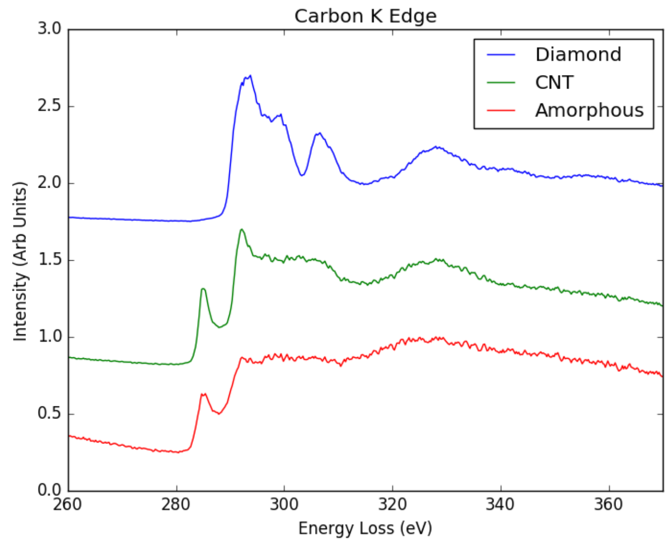

Figure 2.6: Carbon K edge taken at 30keV at McGill. The different crystal structures (amorphous, diamond and carbon nanotube) result in distinctly different ELNES which can be used for identification.

decay in intensity with increasing energy seen in Figure 2.4, limits the useful range ionization edges to those less than ~2keV which corresponds to approximately the K edge of silicon (Z=14) [35]. This upper energy limit is why EELS is better tailored for light elements.

These are the essential principles behind an EELS spectra. In this work, we focus largely on ELNES in lithium materials, and we will now discuss how EELS is performed experimentally.

2.1.2 EELS in Experiment

In order to collect EELS spectra, electrons must pass entirely through the sample, making EELS a technique for transmission electron microscopes (TEM's)[14]. In order to collect these transmitted electrons and divide them according to energy, a magnetic prism is placed below the specimen and redirects the electrons into a detector, Fig 2.7. Inside the magnetic prism, there is a **B** field perpendicular to the beam direction and the transmitted electrons

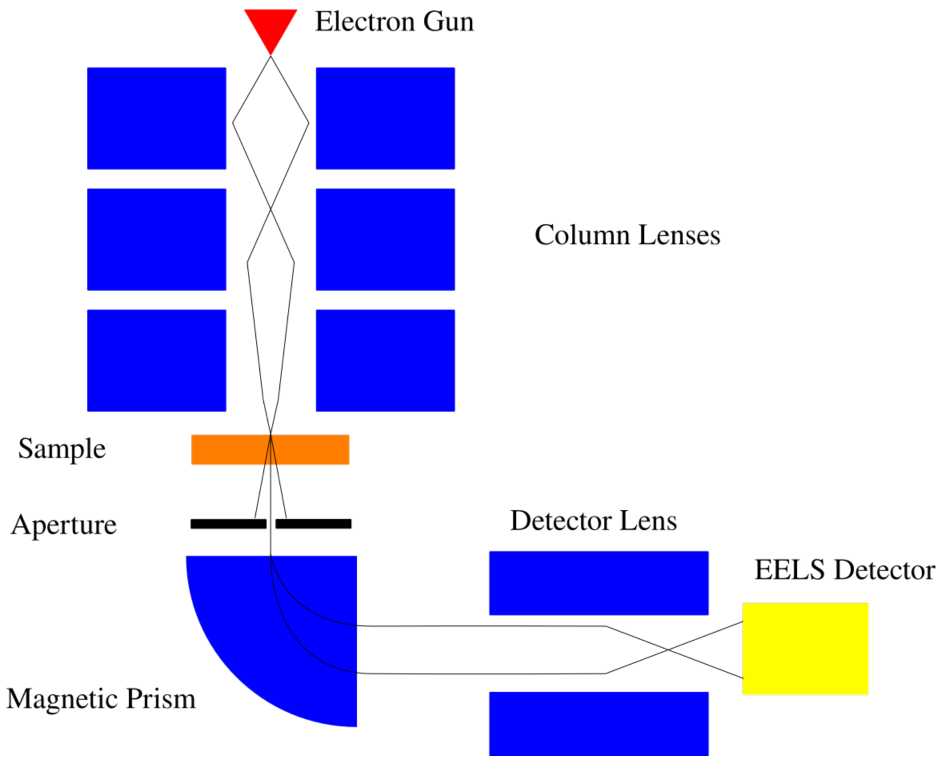

Figure 2.7: Experimental EELS setup, with the various magnetic lenses depicted in blue.

are exposed to a Lorentz force (bold text indicates vector quantities) [36]:

$$\mathbf{F}_B = q(\mathbf{v} \times \mathbf{B}) \tag{2.3}$$

As the force varies according to the velocity of the electrons, the magnetic prism separates the electrons according to their energy:

$$\mathbf{F}_B = e(\mathbf{v} \times \mathbf{B}) = \frac{m\mathbf{v}^2}{\mathbf{r}} = \mathbf{F}_c \tag{2.4}$$

$$r = \frac{mv}{eB} = \frac{\sqrt{2mE}}{eB} \tag{2.5}$$

Where e is the charge of an electron and E is the energy of each electron after passing through the sample. Spectra are obtained by mapping each location on the detector to a corresponding energy loss value. Images are produced by rastering the beam over the sample and using the intensities of a specific energy loss value to create an image.

The quality of EELS results depends numerous factors in the microscope. Foremost among these is the quality of the electron beam. In order to obtain accurate results with regards to the finer features, the beam electrons must have very similar energies before striking the sample, within a few eV. The larger this spread, the worse the energy resolution on the sample which obscures features in ELNES. The energy spread is largely dictated by the electron gun, with the choice for EELS being a field emission gun ($\delta E \sim 0.5 - 1eV$), as older style tungsten and LaB_6 guns are unsuitable for EELS with energy spreads greater than 2 eV [35]. The energy resolution can be further improved to the order of ∼10meV through the use of monochromators [37]. This improved energy resolution however comes at the cost of beam current which is another essential parameter for performing EELS. This is because sufficient signal needs to be collected to render the statistical $\sqrt{N}$ errors small enough for features to become discernible. At higher energies, introducing a monochromators can results in a trade off between experimental error from the beam and statistical errors due to lack of counts. Lower current also translates into longer acquisition times, which expose the sample to more beam damage. In addition to the beam properties, EELS results also depend largely on the imaging mode being used in the electron microscope as is discussed below.

TEM vs SEM EELS

There are two main branches of electron microscopy, scanning and transmission (SEM and TEM). TEM typically operates with beam energies between 100-300 keV designed to penetrate through thin samples, while SEM performs between 1-30 keV targeted towards analyzing bulk samples. Each method has their own set of advantages. The thin samples in TEM's result in a minimal interaction volume, far higher spatial resolution and have the ability to image individual atoms [12]. SEM's scan the surfaces of samples and the large interaction volumes allow them to analyze bulk properties. SEM is also a more economical and flexible technique as it has far fewer sample requirements. EELS has been conventionally performed in TEM's as it requires the beam to pass through the sample and higher beam energies allow for thicker samples. Recent advances however have allowed EELS to be performed in an SEM using accelerating voltages of 30 keV [15]. As in a TEM, EELS in an SEM at 30keV requires thin samples, but offers the advantage of reducing the beam damage which has been essential for investigating lithium materials.

2.1.3 Lithium in EELS

Lithium materials present a number of challenges to EELS analysis. Lithium ion battery materials are in general semiconductors with band gaps of varying sizes. Coupled with lithium's highly mobile nature, lithium materials are highly sensitive to electron beam damage. This damage results from the charge buildup when an electron beam passes through a sample. In electron conductive samples (eg. metals), this charge can be dissipated to a certain extent, however in materials with a band gap (eg. insulators, battery cathodes), this charge can displace lithium ions and break down the crystal structure. Lithium's high mobility also make them vulnerable to knock on damage. This effect occurs when an electron interacts inelastically with an atom's nucleus and transfers sufficient energy to it to displace it from its lattice site. Lithium is particularly vulnerable to this interaction because it requires only a small amount of energy ($\sim 0.2 - 3$eV) to displace it through a crystal [38]. Lithium's sensitivity to the beam make EELS's short acquisition times, on the order of seconds, well suited for its analysis. The recent ability to perform EELS at 30keV has also made it applicable to an entirely new range of lithium materials.

Beyond the experimental essentials, the matter is further complicated by lithium's only ionization edge being located at $\sim$55eV. 55eV is at the boundary of what is considered reasonable for analysis as it lies close plasmon peak. The decay of the plasmon peak complicates background subtraction and makes it highly vulnerable to sample thickness. This energy range also often results in overlap between the lithium K-edge and the $M_{2/3}$ and M_4 edges of transition metals. In particular, the edges of Mn, Fe and Ni, all fall between 40-70eV. As these elements are key components to cathode materials, they can require further steps for analysis to be possible.

2.1.4 Preprocessing

There are two key steps to be performed upon acquiring an ELNES spectra before it can be used for meaningful conclusions, background subtraction and deconvolution.

Background Subtraction

The smooth decaying background in EELS spectra needs to be removed in order for meaningful comparison and measurements to be made on ELNES. However, the EELS background does not decay at a fixed rate and changes based on the presence of edges and with energy [39]. Consequently, it is not currently possible to fit a single function to an entire spectrum. Instead, the method of choice relies on fitting to a window directly before an ionization edge and refitting for each edge as needed. The most prevalent function used for this purpose is a power law decay [14]:

$$I_{bg} = AE^{-r} \tag{2.6}$$

Where E is the energy loss and A and r are fitting factors, typically determined through a least squares procedure [35]. This method has limitations due to different regions of the spectra decaying at different rates, with r ranging from 2-6.5 [35]. A fit must therefore be performed for every feature being analyzed in a spectrum [40; 41]. A downside of this method is the final results dependence on the size and location of the fitting window on the final output, see Fig 2.8. It is further complicated in situations when edges overlap or when attempting quantitative analysis. Coupled with the instability of power law fitting, this has resulted in a number of alternate models, such as polynomials, being proposed for specific cases. The power law method however, remains the most prevalent [40; 42].

Deconvolution

Despite drastic improvements in experimental equipment, there is still a degree of energy spread on beam electrons, typically in the range of ∼0.5-3eV. This energy spread results in

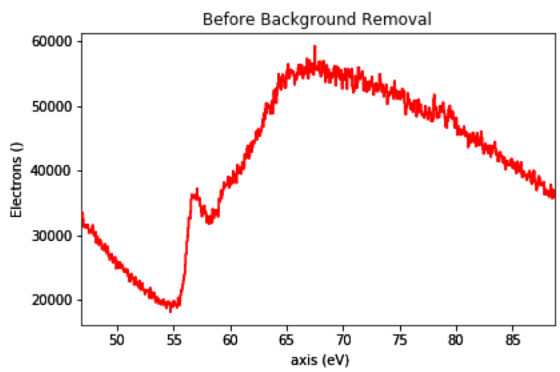

(a)

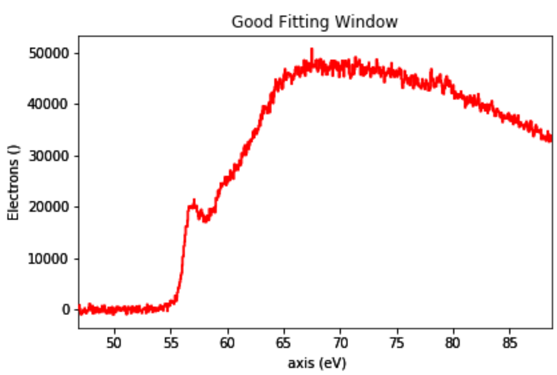

(b)

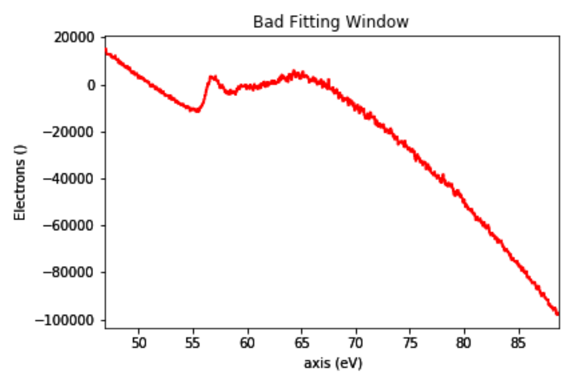

(c)

Figure 2.8: Results of power law background removal from raw spectrum (a) of metallic lithium K edge, using an appropriate (b)and inappropriate (c) window choice.

the observed ELNES on a spectra to be a convolution between the "actual" ELNES and the ZLP. Additionally, the probability plural scattering must also be accounted for, as the low loss region of the spectrum is also convoluted into the output spectra. In order to recover the single scattering spectrum, the output must undergo deconvolution. A number of techniques exist for this purpose which can be split into Fourier and Bayesian methods. Fourier techniques rely on describing the signal as a number of convolutions:

$$J(E) = Z(E)) * [\delta(E) + \frac{S(E)}{I_0} + \frac{S(E) * S(E)}{2!I_0} + ...] \tag{2.7}$$

Where J(E) is the obtained spectra, Z(E) is the zero loss peak, S(E) is the single scattering spectra, and I_0 is the integrated intensity of the zero loss. The double scattering term is the convolution of the two single scattering terms, weighted by the decreased probability according to Poisson statistics. Taking a Fourier transform of this turns all of the convolutions into products:

$$j(\nu) = z(\nu)\left(1 + \frac{s(\nu)}{I_0} + \frac{s^2(\nu)}{2!I_0} + \frac{s^3(\nu)}{3!I_0} + ...\right) \tag{2.8}$$

Which can in turn be collapsed into an exponential:

$$j(\nu) = z(\nu)\mathrm{exp}[s(\nu)/I_0] \tag{2.9}$$

This equation can then be solved for $s(\nu)$ and reverse Fourier transformed to obtain the single scattering spectra. In order to avoid amplifying the noise in the original spectra, which is represented by high frequency terms in Fourier space, the result must be broadened by a modifier to minimize these terms. Thus, deconvolution can only improve the energy resolution of a spectra to a certain extent.

More recently, Bayesian methods have found success as well, in particular the Richardson-Lucy technique [43]. This technique is based on iterative methods initially developed in astronomy and used for the deconvolution of images, including those taken with the Hubble space telescope [44]. From the same starting point, the convolution of the ideal spectra with the low loss, or point spread function ($R(E)$):

$$J(E) = R(E) * S(E) \tag{2.10}$$

As an EELS spectra is inherently pixilated by the CCD, we can turn the convolution into a sum, defining the observed intensity at a pixel based on the intensity of the surrounding pixels:

$$J(i) = \sum_j P(i,j)S(j) \tag{2.11}$$

Where $P(i,j)$ defines how much the intensity at pixel j affects pixel i. From here, the Richardson-Lucy algorithm applies Poisson statistics and iteratively calculates the single scattering spectra as [43]:

$$S^{k+1}(j) = S^k(j)\left(\sum_i \frac{P(i,j)J(i)}{\sum_l P(i,l)S^k(l)}\right) \Bigg/ \left(\sum_i P(i,j)\right) \tag{2.12}$$

Where k is the iteration number. As with Fourier methods, the final spectra cannot gain any more information, increasing iterations results in increased noise and artifacts as well, see Fig 2.9.

2.1.5 Other Experimental Techniques

EELS is by no means the only experimental technique available for the analysis of material microstructure, nor is it even the only electron microscopy technique available for the task. Other prevalent techniques include x-ray based analysis such as x ray absorption spectroscopy and energy dispersive spectroscopy. We will take a moment to briefly describe these methods and compare them to EELS.

X Ray Absorption Spectroscopy (XAS)

XAS operates on a similar principle to EELS. Instead of probing the sample with an electron probe, a beam of x-rays is directed through the sample and the resulting energy losses in the output spectrum are binned as in EELS [45]. The difference in probe media does not effect

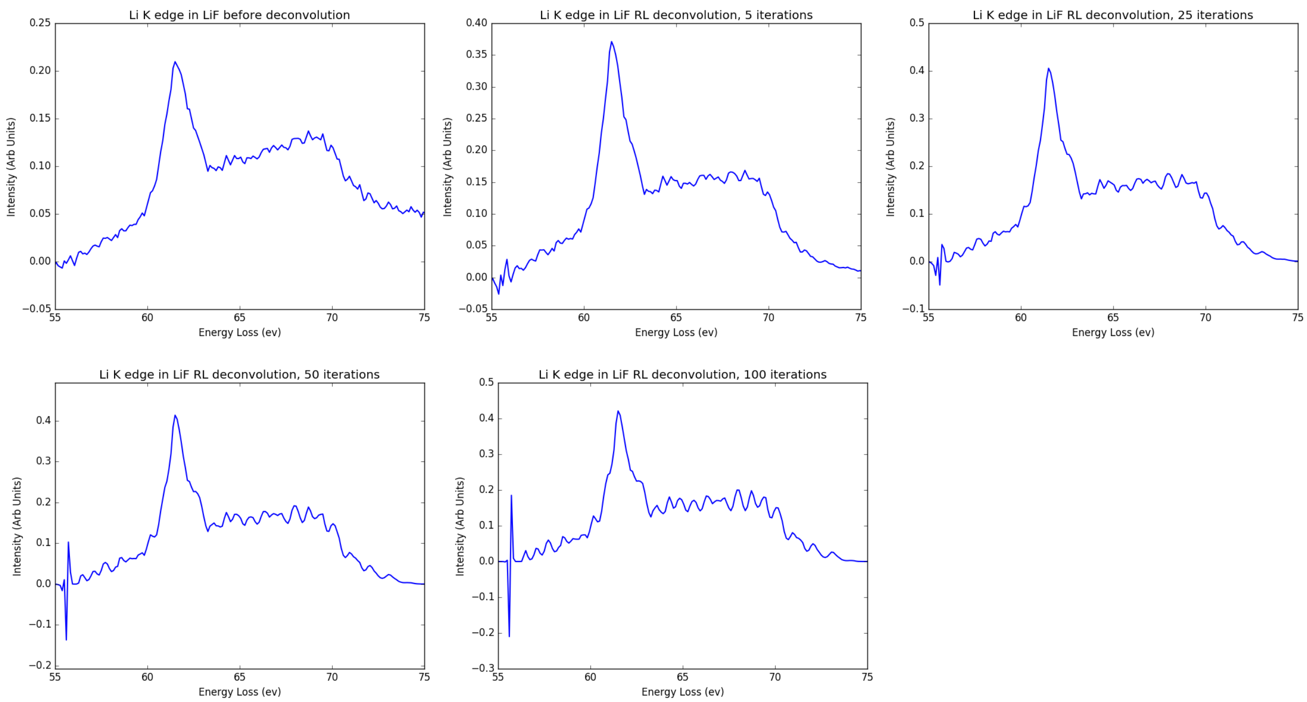

Figure 2.9: Effect of increasing iterations in Richardson-Lucy Algorithm. Iterations increase left to right, starting from the unprocessed background removed spectra on the top left, followed by 5, 25,50, 100 iterations of deconvolution applied.

the measured quantity which is the same as in EELS: the unoccupied density of states of the material [45]. Because of their similarities, parallels have been drawn between EELS and XAS when developing theories. XAS however is typically performed at far higher energies (> 5 keV) and consequently has limited applicability to lithium [46]. The largest benefit of XAS is it's superior energy resolution ($\sim$0.1 eV) when compared to EELS ($\sim$1 eV) allowing for more features in near edge structures to be identified[14; 45]. This benefit comes at a cost however, XAS needs to be performed in a synchrotron, making it far more costly and less accessible to perform than EELS

Energy Dispersive Spectroscopy (EDS)

EDS is another form of analytic spectroscopy performed in electron microscopy. Unlike EELS and XAS which measure the unoccupied density of states, EDS measures the occupied DOS [23]. Like EELS, EDS probes the sample with an electron beam, but then collects the emitted x-rays produced when the sample electrons return to their relaxed states following excitation. These x-rays have the same characteristic energies as in EELS, but EDS lacks the resolution to distinguish fine structure. As such, it is limited to providing composition information on samples. EDS is however less strict on sample requirements as it does not require the thin samples needed by EELS and can therefore be used to analyze both bulk and microscale features in samples [23].

2.2 Density Functional Theory

Many of the results from EELS have non-intuitive interpretations, particularly in the case of ELNES which relies largely on qualitative comparisons between measured and database spectra. Consequently, new materials and situations require a degree of theoretical support to analyze novel results. This support often comes from ab initio calculations, amongst others density functional theory (DFT). This section will describe the basis of DFT and its various implementations, as well as discuss the peculiarities of simulating lithium materials.

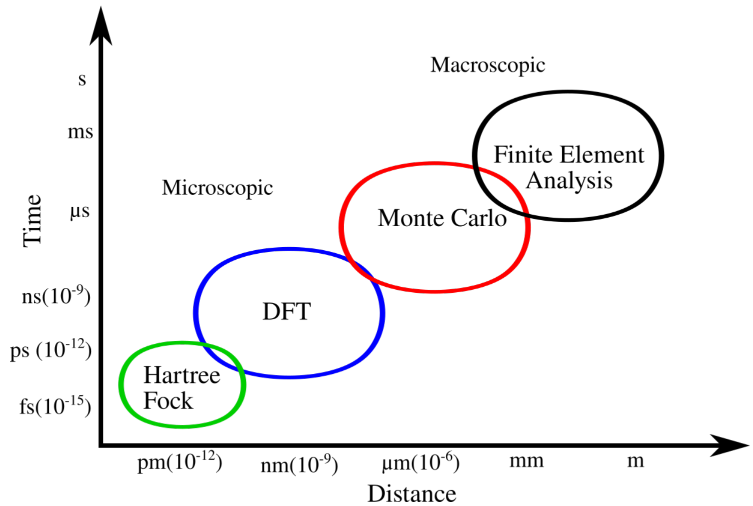

Figure 2.10: Various methods available to compute material properties and their corresponding regions of use.

2.2.1 Background

DFT is an ab initio method that requires only atomic positions as input and is independent of experimental support. By solving a modified version of the Schrodinger equation, it is possible to obtain the ground state energy of the system, and from there determine a range of other properties, including EELS spectra. This almost direct treatment of quantum mechanics make DFT one of the most accurate techniques, however, the quadratic to cubic scaling of the method, limit its applicability to small scale systems, Fig 2.10. DFT's success and flexibility have resulted in the development of a large number (90+) of codes, both open source and commercial, and its place in a wide array of fields [47].

2.2.2 Formulation

DFT is centred on solving the many bodied Schrodinger equation [48]. The aim is to obtain a solution for ψ from which observable properties can be calculated:

$$\frac{-\hbar^2}{2}\sum_{i}^{N}\frac{\nabla^2\psi_i}{m_i}+\sum_{i}^{N}V(\mathbf{r}_i)\psi_i=E\psi \tag{2.13}$$

In this case, we will consider the non-relativistic, spin independent, time independent case, although more in-depth derivations can be found elsewhere [49]. We will now apply the Born Oppenheimer approximation which assumes that the nuclei can be separated from the electrons and will act classically. The validity of this assumption stems from the fact that nuclei are a over 1000 times more massive than electrons [50]. The Born Oppenheimer approximation allows us to only solve for the ψ of electrons:

$$\left[\frac{-\hbar^2}{2m_e}\sum_i^N \nabla^2 + \sum_i^N V(\mathbf{r}_i) + \sum_i^N \sum_{j<i} U(\mathbf{r}_i, \mathbf{r}_j)\right]\psi_i(\mathbf{r}_i) = E\psi_i \tag{2.14}$$

Where m_e is the mass of an electron, N is the number of electrons, and $\mathbf{r}_i$ is a position vector. The terms inside the square brackets are collectively know as the Hamiltonian and are respectively: the kinetic energy of all the electrons, the Coulomb interaction between the electrons and the nuclei, and the electron-electron Coulomb interaction [48]. At this point, these equations are still too unwieldy to solve, depending on 3N variables (the position coordinates of each wavefunction), not to mention the many body problem lurking inside the double sum. Facing this conundrum, we take advantage of the Hohenberg-Kohn Theorems which postulates [51]:

- The ground state *energy* of the system is a unique functional of the ground state *electron density.*
- The electron density that minimizes the overall energy corresponds to the real ground state density.

By changing the variables being solved for to the *density* and not wavefunctions, we can simplify the problem down to only three variables: the three coordinates of the density field. The Hohenberg-Kohn theorems indicate that we can make everything a functional of electron density and that any density other than the groundstate will result in a higher energy in the system [52]. We now define the term functional, as an object that acts like a function, except takes other functions as input instead of variables, eg:

$$F[f(x)] = f(x)^2 \tag{2.15}$$

In the case at hand, the relevant functional is the energy which is a functional of the density: $E[n(\mathbf{r})]$. Using the Hohenberg-Kohn theorems, we can begin working towards a more manageable equation for energy as a functional of density by further breaking down the potentials:

$$-\frac{\hbar}{2m_e}\sum_i \int \psi_i^* \nabla^2 \psi_i d^3r + \int V(\mathbf{r}) n(\mathbf{r}) d^3r + \frac{e^2}{2}\int\int \frac{n(\mathbf{r})n(\mathbf{r}')}{|r-r'|} d^3r d^3r' + E_{\text{nuclei}} + E_{\text{XC}} = E[n(\mathbf{r})] \tag{2.16}$$

Where, the second term is the energy from the electron density-nuclei interaction with $V(\mathbf{r})$ is the electric field created by the nuclei; the third term is the electron density-electron density Coulomb interaction and E_{nuclei} is the contribution from nucleus-nucleus interaction. The final term, E_{XC} is the exchange and correlation term and is where all of the quantum features of the electrons have been grouped; the price to pay for substituting in density. This equation cannot be directly solved from first principles by itself as we need some way to obtain the electron density. On this front we introduce the Kohn -Sham equations which assume that we can decouple all of the electrons into single particle equations:

$$\Big[T_i + V(\mathbf{r}) + V_{\text{H}}(\mathbf{r}) + V_{\text{XC}}(\mathbf{r})\Big]\phi_i(\mathbf{r}) = \epsilon_i \phi_i(\mathbf{r}) \tag{2.17}$$

Where ϕ_i and ϵ_i are the Kohn sham wavefunctions and eigenvalues respectively and V_H is the Hartree potential or:

$$V_{\text{H}} = e^2 \int \frac{n(\mathbf{r'})}{|\mathbf{r} - \mathbf{r'}|} d^3r' \tag{2.18}$$

Which represents the interaction of the electron in question (the one at $\mathbf{r}$, not $\mathbf{r'}$) and all the electrons in the sample. This results in some interaction between the electron and itself, a term that must be corrected for in the V_{XC} term. The Kohn-Sham equations can be readily solved, but require the density to calculate the Hartree potential. The density is in turn given from the wavefunctions:

$$n_{\text{KS}}(\mathbf{r}) = 2\sum_i \phi_i^* \phi_i \tag{2.19}$$

Where the two is to account for electron spin. As the density is needed to calculate the wavefunctions and vice versa, a self consistent approach must be taken in order to obtain a valid result:

1. Assume a starting density

2. Use the initial density to calculate the Hartree potential and use it to solve the Kohn-Sham equations for the wavefunctions

3. Calculate a new density using Eqn. 2.19.

4. Compare the new density to the initial, update the initial density.

5. Repeat steps 2-4 until the density converges and the energy is minimized. This density then represents the groundstate for the system.

This method is the starting point for DFT calculations, from here there are a number of different variations with regards how to go about these steps. Amongst others, the treatment of the exchange-correlation potential and choice of basis for the wavefunctions is what separates the methods.

Exchange-Correlation Potential

The exchange-correlation potential was introduced above, but not defined. That is because there no easily solvable form for this term as it must collect all of the unknown features not accounted for in the rest of the Kohn-Sham equations, including electron's being indistinguishable, the self interaction term, etc. There have been a number of proposed potentials, many designed for specific situations the most common of which will be discussed here. Like the other potentials in the Kohn-Sham equations, the XC potential is defined as a functional of density. The various potentials vary according to accuracy and computational cost. The first attempt, originally proposed by Kohn and Sham in 1965 was the local density approximation (LDA) in which the XC potential depends only on the density [16; 53]:

$$E_{\mathrm{XC}}[n(\mathbf{r})] = \int n(\mathbf{r})\epsilon_{\mathrm{XC}}[n(\mathbf{r})]d^3r \tag{2.20}$$

LDA is exact in the case of a free electron gas and has obtained good success when applied to metallic solids. By considering the gradient of the density as well, a more involved potential is obtained, called the generalized gradient approximation (GGA) [53; 54] :

$$E_{\mathrm{XC}}[n(\mathbf{r})] = \int n(\mathbf{r})\epsilon_{\mathrm{XC}}[n(\mathbf{r}), \nabla n[\mathbf{r}]]d^3r \tag{2.21}$$

Other parameters can also be taken into consideration, such as the potential energy (meta GGA) or empirical factors (hybrid functionals) [53; 55]. Depending on the desired property and available computing power, an appropriate functional should be chosen for each case.

Basis Sets

A second defining feature for DFT is the choice of basis set for the wavefunctions, ϕ_i, and a number of options have become prevalent in the available programs. These are divided into two distinct types, localized and periodic [48]. Localized basis sets rely on using orthogonal functions that decay rapidly away from the origin [48]. An example is Gaussian peaks, as is used in the Gaussian16 software package [56]. The very localized basis set is useful for handling single, isolated molecules, and as such is ideally suited applications in quantum chemistry and biology. Poor scaling with electron number (typically N^3 or worse) limits the maximal size of system that can be studied [57]. In materials science, a typical system of interest is a bulk material and thus unsuitable for this type of approach. To handle these cases, periodic basis sets are used, by defining a unit cell and repeating it infinitely in all directions. The solution to the Schrödinger equation under these periodic boundary conditions is given by Bloch waves, defined as [58]:

$$\psi = u(\mathbf{r})e^{i\cdot\mathbf{k}} \tag{2.22}$$

Consequently, a natural basis choice for periodic boundary situations are plane waves, which are used in a number of DFT packages including VASP, Quantum Espresso, and Wien2k [17; 20; 59]. The periodic boundary method allows for accurate calculation of in infinitely samples representative of bulk materials. Computation limits still apply to the size

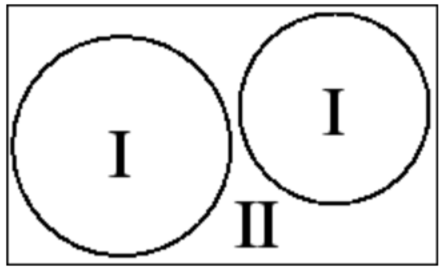

Figure 2.11: The two regions in an APW approach. (I) Atomic Basins modelled with Psudopotentials or atomic orbitals and (II) interstitial space modelled with a plane wave basis set [17].

of the unit cell, typically limited to at most a few hundred atoms [57]. This effect renders features such as defects and grain boundaries highly computationally expensive as they must be contained in a cell large enough to isolate them from their images in adjacent cells. As large numbers of plane waves would be required to handle the fine features in the electron density close to nuclei, often an augmented plane wave (APW) technique is used. APW lowers the computational cost by dividing the unit cell into two regions: interstitial space and atomic basins (sometimes referred to as muffin tins), illustrated in Fig 2.11 [17].

The ability to divide electrons into two groups is due to the fact that the core electrons surrounding each atom are largely unaffected by their local environment as they are screened by the outer shells [17]. The choice of which basis set is used inside the muffin tins provides further options between DFT codes. One option is pseudopotentials, which are pre-generated densities for each element, which can be varied to match the plane waves at the boundary [60]. The pseudopotential method is used in a number of codes, amongst others, VASP and Quantum Espresso [20; 59]. Alternatively, spherical harmonics corresponding to the atomic orbitals can be used for increased accuracy [58]. This type of DFT is referred to as all-electron or full potential, as every electron is represented in the basis set, unlike the pseudopotential method where many are absorbed into the pre-calculated PP [17]. Fitting for all of the electrons in the sample comes at a computational cost, yet allows for more accurate analysis of properties dependent on core states, such as ELNES spectra in EELS.

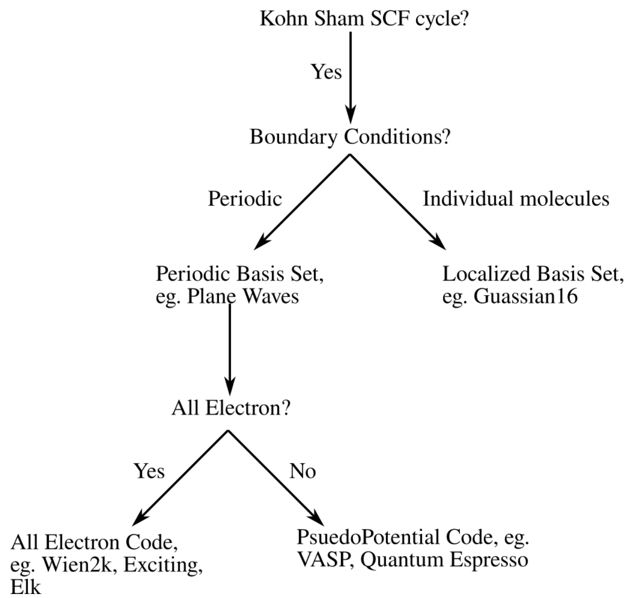

Figure 2.12: Flowchart depicting the various choices of basis set available to DFT codes.

A flowchart demonstrating the various properties of some common DFT codes is presented in Fig 2.12. The DFT code used primarily in this work is Wien2k.

2.2.3 WIEN2k

WIEN2k is an all electron code that uses a linearized augmented plane wave (LAPW) formulation, combining plane waves with spherical harmonics as in Fig 2.11 [17]. In WIEN2k's standard formalism, the basis sets for the Kohn-Sham wavefunctions can be represented as:

$$\phi_{k_n} = \begin{cases} \Sigma_{lm}[A_{lm,\mathbf{k}_n} u_l(r, E_l) + B_{lm,\mathbf{k}_n} \dot{u}_l(r, E_l)] Y_{lm}(\hat{\mathbf{r}}) & r \leq r_{\mathrm{RMT}} \\ \frac{1}{\sqrt{\omega}} e^{i\mathbf{k}_n \cdot \mathbf{r}} & r > r_{\mathrm{RMT}} \end{cases} \tag{2.23}$$

Where $Y_{lm}(\hat{\mathbf{r}})$ are the spherical harmonics and $u_l(r, E_l)$ are the solutions to the radial Schrödinger equation. The coefficients $A_{lm,\mathbf{k}_n}$ and $B_{lm,\mathbf{k}_n}$ are set so as to match the value and slope of the plane waves at the boundary [17]. The use of an all electron code is essential for computing EELS accurately as it allows a more flexible treatment of core electrons not granted in pseudopotential codes.

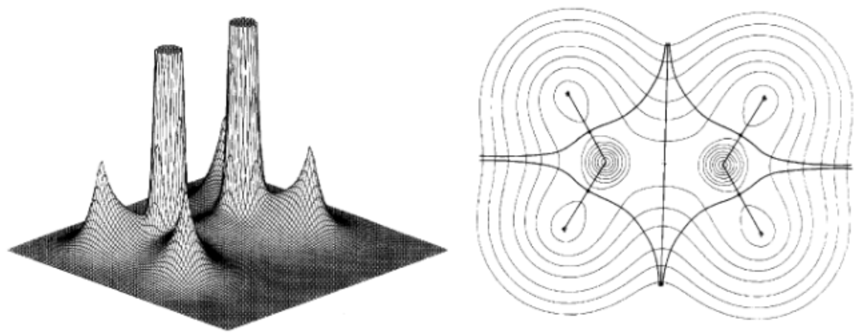

Figure 2.13: Density plot (left) and identification of atomic basin (right) in diborane atomic From Bader [61].

2.2.4 Quantum Theory of Atoms in Molecules

Before continuing to the application of DFT to EELS, we will briefly discuss a more direct application of DFT; defining atoms and bonds from the electron density. Initial work on this front was performed by Bader [61]. The electron density can be divided into regions, with each atomic basin delimited by surfaces satisfying [62]:

$$\nabla\rho(\mathbf{r}) \cdot \mathbf{n}(\mathbf{r}) = 0 \qquad \forall\mathbf{r} \in S(\Omega, \mathbf{r}) \tag{2.24}$$

That is, surfaces with no flux of electron density through them and can be pictured as a “valleys” in the electron density “landscape,” see Fig 2.13. In order to calculate the location of these surfaces, critical points in the density field are located, defined when $\nabla\rho(\mathbf{r}) = 0$, and always satisfy Eq. 2.24. With the exception of critical points at maximas in $\rho(\mathbf{r})$ which are located at nuclei, all of the critical points lie on interatomic surfaces [63]. The nature of the critical points can then be evaluated (minima, first or second order saddle point), and the location of bonds which are centred on first order saddle point critical points, can be determined [63]. The bonds can then be characterized to provide first principles chemical bonding analysis for quantum chemistry [64].

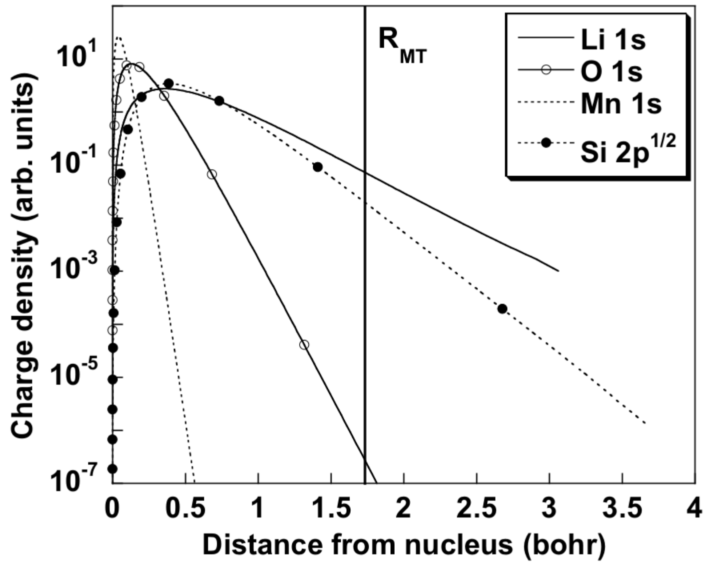

Figure 2.14: Orbital charge densities as a function of distance from nucleus, demonstrating the varying degrees of localization. From Mauchamp et al [21]

2.2.5 Lithium in DFT

As in experiment, lithium's low atomic number requires a number of special treatments in DFT. These are largely due to loosely bound electrons with large orbitals resulting from lithium's small nuclear charge. As a result, even the 1s level electrons in lithium can have orbitals extending well past 2.5 Bohr from the nuclei, far further than in heavier elements, see Fig 2.14 [21]. This results in a number of issues. Firstly, it is difficult and sometimes impossible to set the atomic sphere radii large enough to contain all these 1s core electrons. As atomic spheres cannot overlap, they are typically limited to $\sim$ 2.0 Bohr. Depending on the compound, the sphere size can be further constrained as all the spheres must be roughly the same size (within 30%) [17]. If the sphere sizes are too varied, convergence time and accuracy can deteriorate dramatically. The alternative to large sphere size is to allow a degree ($\sim$0.5%)of core leakage into the calculation [17]. The downside to allowing leakage is that it may result in non physical effects at later stages in the calculation, or result in the appearance of "ghostbands" in the calculation [17].

2.3 EELS Calculations

Having described the inner workings of EELS and DFT, we will now investigate how we can use the ground state density and the Kohn-sham wavefunctions and eigenvalues to calculate the features of an EELS spectra. Central to this challenge, is the fact that DFT is however a ground state theory; the Hohenberg Kohn theorems only guarantee that agreement between the calculation and reality for the lowest energy state [51]. As EELS inherently involves exciting an atom above this ground state, a number of assumptions must be made to address this issue. The various approaches to the issue of handling excitations are defining features of many of the techniques used to calculate EELS. Additionally, the varying requirements of the wide array of features in EELS spectra further diversify the techniques. Broadly, there are three methods for calculating EELS: multiple scattering, atomic multiplet and band structure methods. We will focus on a number of the band structure methods as well as their advantages and applicability below.

2.3.1 Time Dependent Density Functional Theory -TDDFT

In TDDFT, the EELS spectrum is computed through the macroscopic dielectric function (ϵ_{M}). As is the case with many EELS calculations, we begin from Fermi's Golden Rule, and define matrix elements which determine the probability of an electron being driven to a new state by some propagator:

$$M_{nm\mathbf{k}} = \langle n\mathbf{k}|e^{-i(\mathbf{q}+\mathbf{G})\mathbf{r}}|n'\mathbf{k}+\mathbf{q}\rangle \tag{2.25}$$

Where $\mathbf{q}$ is the momentum transfer from the beam to the sample and $\mathbf{G}$ is the Fourier coefficient of the probe. The initial and final states are the key parameters taken from DFT [19]. These matrix elements can be used to determine the independent particle polarizability χ^{KS} [19]:

$$\chi^{\mathrm{KS}}_{\mathbf{G},\mathbf{G'}}(\mathbf{q},\omega) = \frac{1}{V}\sum_{nm\mathbf{k}} \frac{f_{n\mathbf{k}} - f_{m\mathbf{k}+\mathbf{q}}}{\epsilon_{n\mathbf{k}} - \epsilon_{m\mathbf{k}+\mathbf{q}} + \omega + i\delta} M_{nm\mathbf{k}}(\mathbf{q},\mathbf{G}) M^{*}_{nm\mathbf{k}}(\mathbf{q},\ \mathbf{G'}) \tag{2.26}$$

Where $f_{n\mathbf{k}}$ is the fermi distribution and V is the volume of the cell. χ^{KS} can be related to the reducible polarizability through the Dyson equation:

$$\chi = \chi_{\mathrm{KS}} + \chi_{\mathrm{KS}}(\nu + f_{\mathrm{xc}})\chi \tag{2.27}$$

Where f_{xc} is the exchange and correlation potential. A common approximation is to set this to zero, a method called the Random Phase Approximation (RPA) [65]. At this point we also make two more approximations. We first assume that $\mathbf{q} \to 0$, referred to as the optical limit. This assumes that the momentum transfer to the sample is minimal, an approach that is valid for low energy losses (<50 eV). We also assume that the probe wavelength is much larger than the resulting perturbations, ($\mathbf{G} \to 0$). This is know as ignoring local field effects. Both of these approximations can be relaxed on a case by case basis, however this comes at increased computational cost [19]. With these approximations, we can proceed to calculate first element of the dielectric tensor:

$$\epsilon_{00}^{-1}(\mathbf{q}, \omega) = 1 + v\chi \tag{2.28}$$

from which we can calculate the macroscopic dielectric function which relates to the energy loss function:

$$[\epsilon_{\mathrm{M}}(\mathbf{q}, \omega)]^{-1} = \epsilon_{00}^{-1}(\mathbf{q}, \omega) \tag{2.29}$$

$$L(\mathbf{q}, \omega) = -\mathrm{Im}[\epsilon_{\mathrm{M}}(\mathbf{q}, \omega)]^{-1} \tag{2.30}$$

The energy loss function is what is directly measured by EELS and is the standard of comparison for TDDFT. TDDFT is accurate for low losses, so ideal for calculations of plasmons, and in the limit of the optical approximation low energy M edges of transition metals and the lithium K edge [22]. Limitations of the approach are that it is based on the final state rule, and thus is susceptible to excitonic effects in $\langle f|$. Additionally, local field effects can require subtle interpretations and come at computational cost to include [22]. TDDFT is also applicable to x-ray absorption spectroscopy where the optical limit is more valid. The only required modifications to the theory are a modification to the propagator in Eq. 2.25 [66]:

$$e^{i\mathbf{q}\cdot\mathbf{r}} \rightarrow e^{i\mathbf{k}\cdot\mathbf{r}}\epsilon\cdot\mathbf{r} \tag{2.31}$$

2.3.2 Cross Section Approach

TDDFT is a suitable choice for low loss EELS. For higher energy ionization edges with non-negligible momentum transfer, Fermi's Golden Rule can be used to compute a double differential cross section instead of the dielectric function. The differentials are with respect to energy and scattering angle, the two relevant parameters in an EELS experiment. The relationship is given by [67]:

$$\frac{\partial^2\sigma}{\partial\Omega\partial E} = \left[\frac{4\gamma^2}{a_{0^2 q^4}}\right]\frac{k_f}{k_i}\sum_{i,f}|\langle f|e^{i\mathbf{q}\cdot\mathbf{r}}|i\rangle|^2\delta(E - E_f + E_i) \tag{2.32}$$

Where a_0 is the Bohr radius, E the energy loss and $\gamma = \sqrt{1-\beta^2}$, the relativistic factor. As in TDDFT, the approach can be modified to solve for XAS, by replacing the Rutherford cross section with the Thompson cross section in the prefactor and changing the propagator according to Eqn. 2.31.

The cross section formalism can also be modified to account for anisotropic samples as well as some experimental parameters [67]. Similar to TDDFT, the essential parameters are the initial and final states, taken from DFT ($\langle f|$ and $|i\rangle$). The simpler approach with fewer approximations can be attributed to the states being investigated: in low loss EELS, both the initial and final states depend heavily on the band structure, whereas for core losses the initial states are relatively constant and well defined [67]. Cross section methods however still suffer from the limitations of a one particle final state rule approach and their lack of ability to deal with excitonic effects.

2.3.3 Beth Salpeter Equations -BSE

The largest drawback of TDDFT and cross section calculations is the single particle formalism, which prevents proper treatment of excitonic effects. Solving the BSE is a two particle method that rigorously calculates the interaction between the excited electron and the resulting hole in the core state [68]. It is applicable to both low and core loss EELS calculations [19]. The core of the BSE is in solving the eigenvalue problem involving the effective two particle Hamiltonian [69]:

$$\hat{H}_{\mathrm{eff}} \left| A_\lambda \right\rangle = E_\lambda \left| A_\lambda \right\rangle \tag{2.33}$$

The effective Hamiltonian can be broken into three parts, the diagonal, exchange and correlation components[69].

The diagonal component which accounts for single particle transitions:

$$H^{(\mathrm{diag})}_{vc\mathbf{k},v'c'\mathbf{k'}} = (\epsilon_{c\mathbf{k}} - \epsilon_{v\mathbf{k}})\delta_{vv'}\delta_{cc'}\delta_{\mathbf{kk'}} \tag{2.34}$$

The exchange component which accounts for the repulsive interaction between the excited electron and its hole:

$$H^{(\mathrm{x})}_{vc\mathbf{k},v'c'\mathbf{k'}} = \int d^3\mathbf{r} \int d^3\mathbf{r'} \varphi_{v\mathbf{k}}(\mathbf{r})\varphi^*_{c\mathbf{k}}(\mathbf{r})\bar{v}(\mathbf{r},\mathbf{r'})\varphi^*_{v'\mathbf{k'}}(\mathbf{r'})\varphi_{c'\mathbf{k'}}(\mathbf{r'}) \tag{2.35}$$

Where φ are the single particle states of the hole and electron and $\bar{v}$ is the unscreened Coulomb potential. Thirdly, there is the correlation component accounting for the attractive interaction between hole and electron:

$$H^{(\mathrm{c})}_{vc\mathbf{k},v'c'\mathbf{k'}} = -\int d^3\mathbf{r} \int d^3\mathbf{r'} \varphi_{v\mathbf{k}}(\mathbf{r})\varphi^*_{c\mathbf{k}}(\mathbf{r})W(\mathbf{r},\mathbf{r'})\varphi^*_{v'\mathbf{k'}}(\mathbf{r'})\varphi_{c'\mathbf{k'}}(\mathbf{r'}) \tag{2.36}$$

Where W is the screened Coulomb potential on the hole. By treating the hole created by the excited electron as a particle, solving the BSE produces vastly superior results to single particle approaches, particularly in those with moderate screening [69]. However, this method is vastly more computationally demanding and can only be performed on the simplest of structures. This large computational trade off has led to the continued prevalence of single particle techniques.

2.3.4 Core Hole Approximation

The computational cost of the BSE method and the difficulties in handling excitonic effects in the single particle approaches has resulted in further approximations being made to improve single particle results. The most significant of these is the core hole approximation. This approximation is centred on artificially exciting a DFT into an excited one in order to better calculate the final states in EELS, $\langle f|$. Early implementations involved replacing the excited atom with the next element on the periodic table, called the Z+1 approach [70]. This method was mildly successful, however it lacks the flexibility to handle excitations from different shells, and has since been largely replaced with the core hole approximation [67]. The core hole approximation involves manually decreasing the occupancy of an excited state, and adding the additional charge to the background to conserve electron number [17]. The effectiveness of the approximation however has been mixed. In some cases, including a core hole results in excellent agreement with experiment, whilst in others, ignoring a core hole produces more accurate results. There have been a number of offered explanations based on the nature of the material: eg. insulators require a hole and metals do not. These general rules have not been successful in predicting all cases and more involved techniques based on density of states maps have also been proposed [71]. In general however, spectra tend to fall in between the two extremes, which has led to some *ad hoc* approaches of including non integer core holes, so as to best fit experiment, see Fig 2.15 [67; 72–74]. This state of affairs has remained unchanged for the past 30 years and consistently leads to unsatisfying results [75–86].

The treatment of core holes is particularly problematic in lithium as core state are very shallow with only a single other core electron to shield it. The shallow shielded hole means that every lithium compound will exhibit some degree of core hole effects. Consequently, in order to calculate lithium ELNES a more rigorous approach to core hole screening is required. Developing a deterministic method of introducing non-integer core holes for this end is the focus of this work

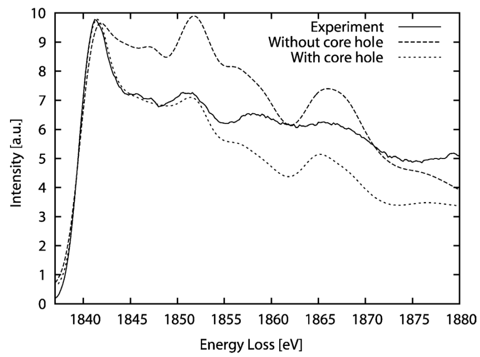

(a)

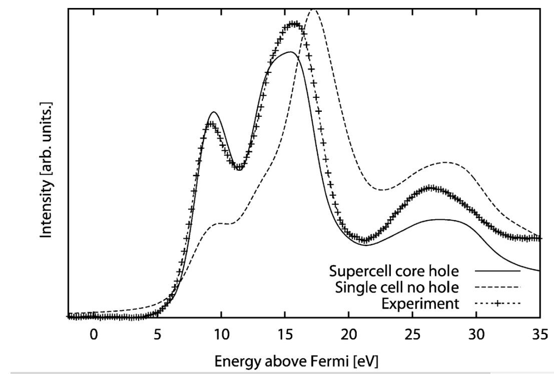

(b)

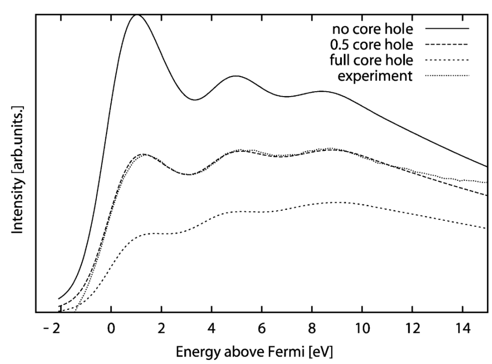

(c)

Figure 2.15: The three typical results of inserting a core hole. In (a) the core hole results in good agreement with experiment. In (b) and (c), the core hole overestimates the excitonic effects, resulting in errors in peak intensity. In (c), an *ad hoc* fractional core hole is inserted resulting in good agreement at the cost of physicality. Results from [73] (a,b) and [72] (c).

Chapter 3

Shielding Calculations

The lack of flexibility and accuracy of the core hole approximation combined with the computational deterrent of solving the BSE presents a barrier to expanding EELS calculations.

Any means of addressing the core hole approximation must satisfy two criteria. First, it must remain a first principles method and not rely on any empirical data. This is essential to be able to investigate unstudied materials. Second, computational cost must remain reasonable and not scale any worse than DFT with the size of the unit cell.

Due to their small atomic number, lithium materials are particularly susceptible to these effects. At the same time however, the few electrons involved with lithium help simplify the issue and thus make it an optimum target for improved methods. In this work, a means to extend these barriers was developed by creating a method to perform a first order calculation of shielding effects from the electron density. In this chapter we discuss the formulation and implementation of this method.

3.1 Core Hole Shielding Calculations

Our goal is to focus on the ionization edges of lithium calculated rapidly enough to be practical in interpreting novel EELS results. To this end, we use the cross section method under the relativistic single particle approach using the final state rule (FSR), Eq. 2.32[87]:

$$\frac{\partial^2\sigma}{\partial\Omega\partial E} = \left[\frac{4\gamma^2}{a_{0^2 q^4}}\right]\frac{k_f}{k_i}\sum_{i,f} |\langle f|e^{i\mathbf{q}\cdot\mathbf{r}}|i\rangle|^2\delta(E - E_f + E_i) \tag{3.1}$$

As mentioned in Section 2.3.4, shielding effects are contained in the $\langle f|$ term. These effects originate from changes in the Hamiltonian caused by introducing a core hole and manifest themselves when solving for $\langle f|$ in the Kohn Sham equations (Eq. 2.17) [88]:

$$\left[T_i + V_{\text{ext}}(\mathbf{r}) + V_{\text{H}}(\mathbf{r}) + V_{\text{XC}}(\mathbf{r})\right]\phi_i(\mathbf{r}) = \epsilon_i\phi_i(\mathbf{r}) \tag{3.2}$$

The core hole alters the Hartree and the exchange and correlation potentials, and this effect is reduced somewhat by shielding. The total change in the potential due to introduction of a core hole can be expressed as:

$$\Delta V_{\text{tot}}(\mathbf{r}) = \Delta V_{\text{H}}(\mathbf{r}) + \Delta V_{\text{XC}}(\mathbf{r}) = V_{\text{CH}}(\mathbf{r}) - V_{\text{S}}(\mathbf{r}) \tag{3.3}$$

where $V_{\text{CH}}(\mathbf{r})$ is the potential of a core hole and $V_{\text{S}}(\mathbf{r})$ represents the shielding potential. The current convention in literature when performing core hole calculations is to ignore this shielding term, despite the large effects it has been shown to have on ELNES. We can break the shielding potential into two parts, core electron and valence electron shielding, $V_{\text{c}}(\mathbf{r})$ and $V_{\text{v}}(\mathbf{r})$. Core shielding is due to electrons occupying core orbitals on the excited atom reducing how much the core hole can be "felt" outside of the atom. Valence screening is caused by valence and interstitial electrons being attracted to the positively charged hole. Neither of these terms are readily solvable for using current methods. At this point, an advantage of lithium's low atomic number becomes clear: as there is only one core electron that could shield the hole, we can assume that core electron screening is negligible, which simplifies this problem considerably.

In order to calculate the valence screening we turn to linear response theory, as $\Delta V_{\text{H}}(\mathbf{r})$ and $\Delta V_{\text{XC}}(\mathbf{r})$ cannot be computed exactly [89]. We begin by considering the change in electron density resulting from the introduction of a core hole, as described by Shirley, Soininen and Rehr [89]:

$$\Delta n(\mathbf{r}) = \int d^3\mathbf{r'}\chi^0(\mathbf{r},\mathbf{r'};\omega=0)\Delta V_{\text{tot}}(\mathbf{r'}) \tag{3.4}$$

Where χ^0 is the irreducible polarization function, given by $\chi^0(\mathbf{r}) = \delta n(\mathbf{r})/\delta V(\mathbf{r})$. At this point, we will proceed in assuming no screening ($V_{\text{S}}(\mathbf{r}) = 0$) and then reintroduce screening later in the form of a perturbation. We also restrict our view to only the excited atom, which in this case gives:

$$\Delta n_{\text{basin}} = \int_f d^3\mathbf{r} n_f(\mathbf{r}) - \int_i d^3\mathbf{r} n_i(\mathbf{r}) = -1 \tag{3.5}$$

Where the basin defining the integration limits is defined by Bader theory as described in Section 2.2.4. This equation indicates that, when there is no screening, the excited core electron has entirely left the basin, with no response from the material. If we now assume that the polarization is constant inside this basin, we can calculate it as:

$$\frac{\Delta n_{\text{basin}}}{V_{\text{CH}}} = \chi^0_{\text{basin}} = \frac{\Delta n_{\text{basin}}}{\Delta V_{\text{tot}}} \tag{3.6}$$

If we further assume that the polarization is constant through changes in shielding potential, we can reintroduce the shielding term and perturb the right hand side of Eq. 3.6 to obtain:

$$\frac{-1}{V_{\text{CH}}} = \frac{-1+\delta n_{\text{basin}}}{V_{\text{CH}} - \delta V_{\text{v}}} \tag{3.7}$$

Which can be reduced to:

$$\frac{\delta V_{\text{v}}}{V_{\text{CH}}} = \delta n_{\text{basin}} \tag{3.8}$$

This equation allows connects the screening due to valence electrons to a change in electron density, a rapidly calculable quantity. The screening potential is given in "units" of the core hole potential which allow the screening to be accounted for by modulating the occupancy of the core hole state. Additionally, while we perturbed from the no screening case in Eq 3.7, it should be noted that this argument holds when approached from the full screening case. This indicates that these approximations should hold over the entire range of screening cases ($\delta V_{\mathrm{v}} = 0 \to V_{\mathrm{CH}}$). We will now discuss how this theory can be implemented into EELS calculations.

3.2 Implementation

Having determined a means of calculating the core hole shielding effects, we describe how these were implemented into ELNES calculations. We begin by performing a standard DFT calculation with no core hole, followed by one including a full core hole. Depending on cell size, the full core hole calculation is performed using a supercell so as to isolate individual core holes in the periodic boundaries. For both calculations, the electron occupancy inside the lithium atomic basin is calculated and used to calculate the screening potential according to Eq 3.8. This returns a decimal value between 0 and 1 which is subtracted from the magnitude of the hole. A third calculation is then performed with using this non integer "shielded" hole, again using supercells as necessary.

Chapter 4

Results and Discussion

Having developed a method and the means to implement it, we now apply it to a number of cases of lithium materials. We choose three common lithium compounds with a variety of properties; metallic lithium, ionic LiF, and covalent Li_2O. We also analyze a mixed compound obtained after observing beam damage on LiF during a transformation into metallic lithium, which we will also discuss.

Before discussing specific cases, it should be noted that all calculations were run in a manner to account for the peculiarities of lithium in DFT. In particular, atomic sphere radii on the lithium were maximized to minimize core leakage and monopole effects were verified to be negligible. The standard DFT convergence tests (K points, RKMax) were also performed and all cells were relaxed according to volume. All supercells were performed in *P1* symmetry so as to only produce a single core hole atom per cell.

All of the experimental results were obtained at McGill on a Hitachi SU900 TE-SEM. Spectra were acquired at 30 keV to minimize the beam damage to the lithium. All spectra had their backgrounds removed through a power law fit (see Section 2.1.4) and were deconvoluted using the Richardson-Lucy algorithm (also Section 2.1.4).

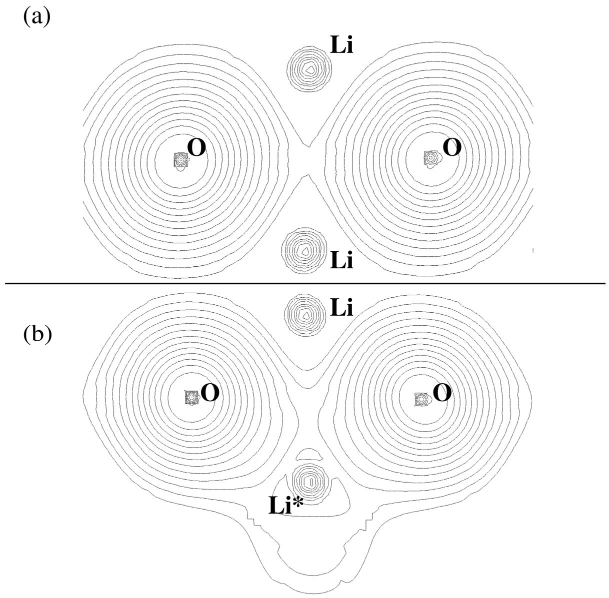

Figure 4.1: Effect of introducing a core hole in Li2O. (a) no hole crystal. (b) Crystal with hole on starred lithium atom, inducing a response from the valence electrons. Contour lines on a logarithmic scale.

4.1 Lithium Oxide

We begin by investigating Li_2O. Screening calculations were performed as described in Section 3.2. After the initial two calculations, (with no hole then full hole), the density around the excited lithium atom was plotted, see Fig 4.1.

The density plots clearly show valence electrons in the material being attracted to the excited atom. This indicates that the core hole should have both a noticeable effect on the final states and that it is screened as well. We can also see that even the closest lithium atom is largely unaffected by the core hole, in agreement with the supercell size being sufficient to isolate core holes. Calculating the difference in electron occupancy shows a decrease of 0.88 electron in the basin. This decrease is smaller then would be expected the no screening limit and according to Eq 3.8, indicates that the hole is 12% screened. A third calculation was then performed using a decreased hole size to obtain a final spectra. The ELNES K edge from all three simulations are compared to experiment in Fig 4.2.

	Ratio	Error
Experiment	0.71	-
Full Hole	0.85	20%
Screened Hole	0.66	6%

Table 4.1: The ratio of intensities in the Li_2O spectra between the two peaks at 55 eV and 58 eV. Errors were calculated relative to experiment.

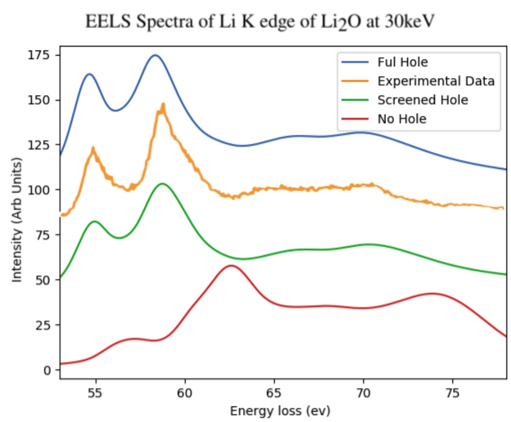

Figure 4.2: Lithium K edge of Li_2O from the three calculations taken with varying degrees of core hole.

From the comparison to experiment, we can observe that the full hole provides good agreement, as previously predicted in the literature [21]. However, the screened hole provides a superior result, which can be emphasized by considering the ratio of the two peaks at ~55eV and ~58 eV. Quantitatively comparing the values, presented in Table 4.1, reveals a dramatic improvement, decreasing the error from 20% to 6%. The qualitative and quantitative improvements to the results support the validity of the new method and highlights it's necessity.

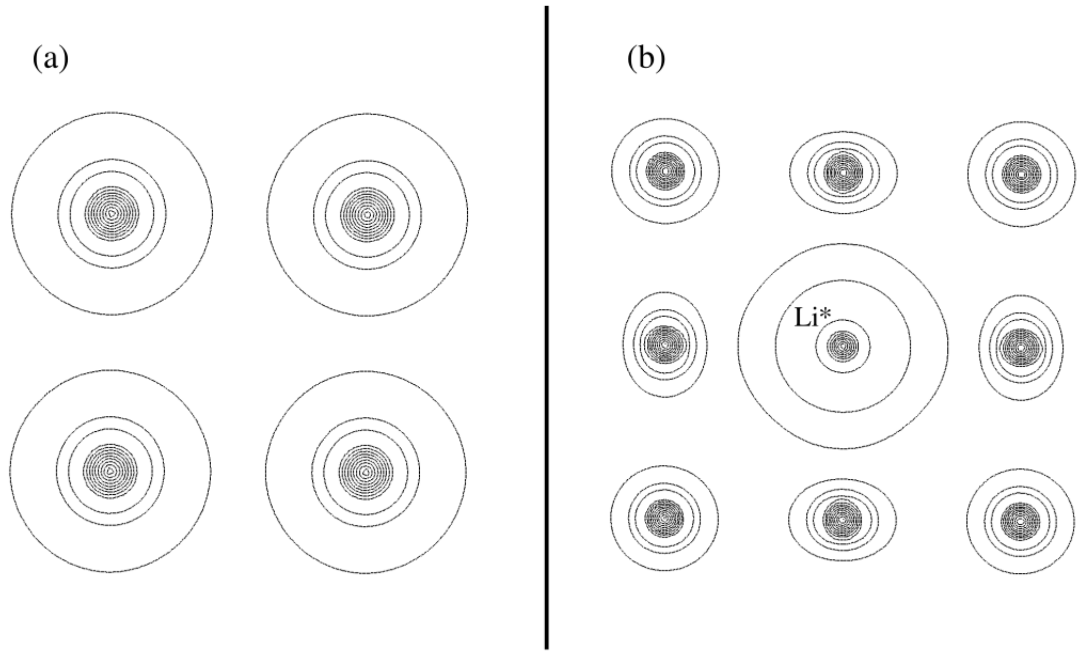

Figure 4.3: Electron density map of metallic lithium, before (a) and after (b) introduction of a core hole on the starred atom. The contours are on equal logarithmic scales.

4.2 Lithium

We now shift our attention to metallic lithium, which has previously presented a number of challenges to experimental analysis. As a metal, it has been predicted to exhibit no core hole effects due to valence screening, and a density plot reveals that core holes have a large impact on the electron density, see Fig 4.3, supporting the notion that the hole may indeed be entirely screened. The excited atom attracts a number of valence electrons and distorts the electron clouds of the surrounding atoms more aggressively than in Li_2O. Calculating the screening factor however reveals that the lithium core hole is in reality only $\sim$41% screened. A comparison with experimental spectra confirms this fact, Fig 4.4.

Again, the literature result assuming no hole provides better agreement than the full hole, but is inferior to the screened hole result. Of particular note is the small peak located at $\sim$58 eV, which is underestimated, in the no hole spectra, overestimated in the full hole, and correctly accounted for in the screened case. The only moderate (41%) screening goes

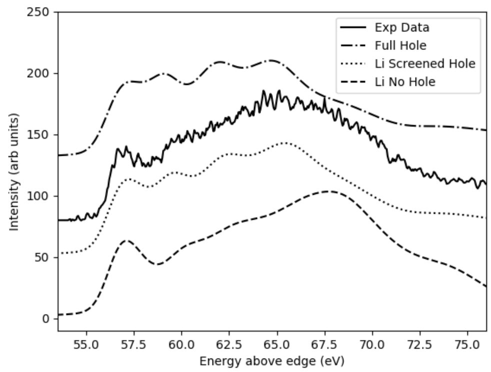

Figure 4.4: Lithium K edge of Li from the three calculations taken with varying degrees of core hole.

against common convention in the literature that metals do not exhibit core hole effects. A couple of more extreme cases have been highlighted (Cu, Al?), but the slight yet significant improvements observed with lithium suggest that screened core holes should be included or at least calculated in all cases. It should be noted that lithium's lack of core electron screening may also contribute to the large core hole effects, which could be lessened for heavier elements.

4.3 LiF

We continue our investigation of pure molecules by considering LiF. LiF has been one of the more published EELS results for lithium and simulations have obtained good agreement with a full core hole approximation [21]. We again begin with a qualitative probe of the electron density, see Fig 4.5. We can see that the introduction of a hole has minor effects on the electron density, but these are largely limited to slight distortions in the fluorine electron cloud, see Fig 4.5. Additionally, despite the loss of a core electron, the density around the excited lithium atom retains much of its initial form. The minimal effect of introducing a core is reflective of fluorine's high electronegativity which "freezes" all of the electrons in place and minimizes any kind of valence electron screening. This effect is confirmed by calculating

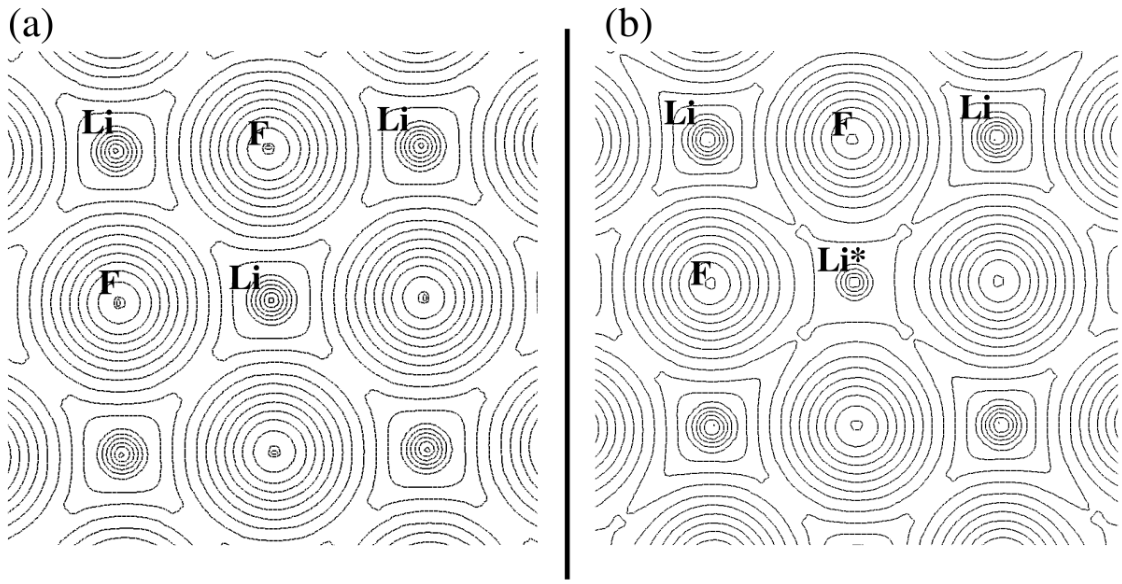

Figure 4.5: Electron density map of LiF, before (a) and after (b) introduction of a core hole on the starred atom. The contours are on equal logarithmic scales.

the screening coefficient which was determined to be zero in this case. Consequently, LiF represents the no screening case of Eqn. 3.5 and we can take the full hole spectra as the final spectrum. Plotting the spectra against experiment confirms that a full hole does indeed produce good agreement, Fig 4.6. The lack of screening in LiF also explains the good results obtained in literature when using only a full hole. It also supports the theory that inserting a full hole is sufficient in the case of strong insulators, although again, lithium's lack of core screening limit the generality of that statement.

4.4 Li-LiF Mixture

We will conclude the results section with a case that demonstrates the full importance of accounting for screening in ELNES calculations. When obtaining the spectra for LiF, we observed a transformation to metallic lithium, due to the beam damage. During this transformation, an intermediate spectra was acquired. To investigate the transformation, a linear combination of the spectra from metallic lithium and LiF was compared to the

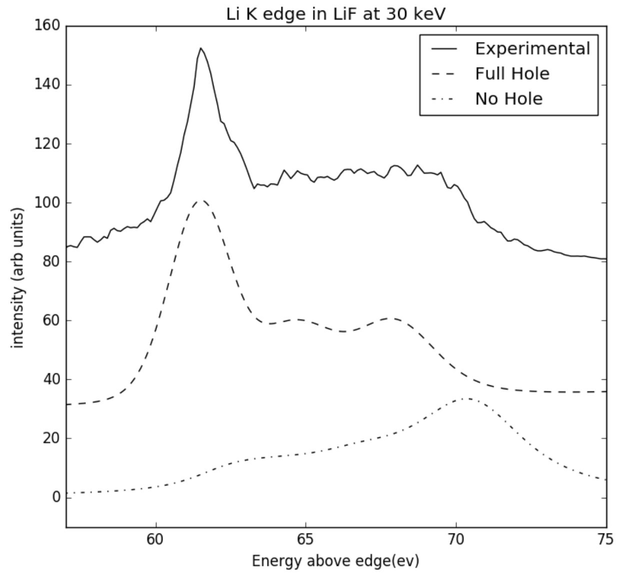

Figure 4.6: Lithium K edge of LiF from the two calculations taken with varying degrees of core hole.

experimental result, see Fig 4.7a. The good agreement obtained here supports both the inclusion of screening and that the sample contains Li, LiF, and no intermediate phases or contamination. The importance of screening is highlighted in Fig 4.7b, where the no hole lithium spectra is used, resulting in a poorer fit, that fails to reproduce the peak at 59eV. This unaccounted for peak would prevent such an analysis from confirming the purity of the sample and of the mixture.

4.5 Discussion

The cases handled here highlight the importance of including a core hole and calculating screening effects when performing ELNES on lithium. In every case, a core hole was necessary, including metallic lithium which had been predicted to not exhibit core hole effects. Additionally, in every case except LiF, screening was non negligible and the first order method developed in Chapter 3 result in dramatic improvements to experimental agreement. The impact of including screening in ELNES calculations is made more apparent when dealing

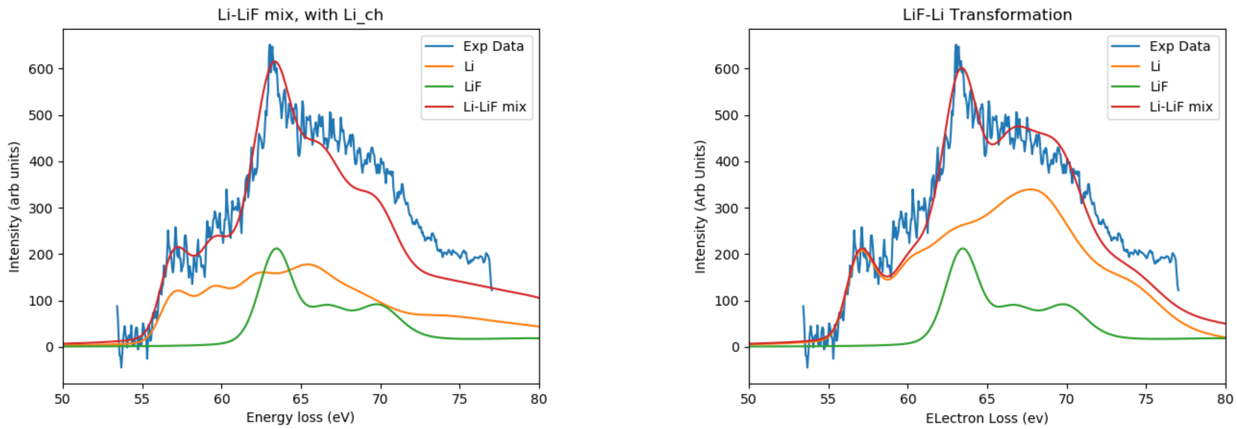

(a) (b)

Figure 4.7: Lithium K edge of Li-LiF mix using full hole LiF spectrum and screened (a) and unscreened (b) Li spectrum.

with unknown cases such as the Li-LiF mixture where it was essential to fingerprinting the near edge structure. The improvement to the peak ratio in Li2O is another key feature in terms of identifying oxidation on lithium edges, or taking the steps to quantitative analysis. Finally the reliable agreement between calculation and experiment help solidify the validity of the technique of performing EELS at 30keV to analyze beam sensitive materials, a result with considerably less weight without excellent agreement between the results.

Chapter 5

Conclusion

The objective of this work has been to develop a means to better simulate ELNES spectra in the context of lithium materials and further verify the reliability of EELS at 30 keV. Lithium's sensitive nature has required the development of new experimental techniques which in turn have produced previously unattainable results requiring a more subtle approach than the literature standard. The new method used to calculate core hole screening is particularly applicable to lithium with its lack of core electron screening. Lithium is also always sensitive to this effect, as seen with the limited amount of core hole screening in metallic lithium.

The second main objective of this work was to highlight the need of further improvements to how ELNES spectra are approached in general. The two largest areas of potential for theoretical calculations lie in their ability to quantify data and to explain and predict unknown results. The current method in literature struggles to achieve either of these goals, and much of their success can be attributed to special case, as was demonstrated such as LiF. In all of the other results, the inclusion of screening effects changed the analysis from being close enough to a far more exact agreement, quantifiable in the case of Li_2O and predictive for the Li-LiF mixture.

The method is currently limited to the lithium K edge, where core electron screening effects can safely be ignored. However, as the results have shown, a more general screening approach is required for the full potential of ELNES simulations to be achieved. .

Chapter 6

Bibliography

[1] Naoki Nitta, Feixiang Wu, Jung Tae Lee, and Gleb Yushin. Li-ion battery materials: present and future. *Materials Today*, 18(5):252–264, June 2015.

[2] Linda Gaines. The future of automotive lithium-ion battery recycling: Charting a sustainable course. *Sustainable Materials and Technologies*, 1-2:2–7, December 2014.

[3] Daniel H. Doughty and E. Peter Roth. A General Discussion of Li Ion Battery Safety. *The Electrochemical Society Interface*, 21(2):37–44, January 2012.

[4] P. G. Balakrishnan, R. Ramesh, and T. Prem Kumar. Safety mechanisms in lithium-ion batteries. *Journal of Power Sources*, 155(2):401–414, April 2006.

[5] Vinodkumar Etacheri, Rotem Marom, Ran Elazari, Gregory Salitra, and Doron Aurbach. Challenges in the development of advanced Li-ion batteries: a review. *Energy & Environmental Science*, 4(9):3243–3262, 2011.

[6] Xia Lu, Liang Zhao, Xiaoqing He, Ruijuan Xiao, Lin Gu, Yong-Sheng Hu, Hong Li, Zhaoxiang Wang, Xiaofeng Duan, Liquan Chen, Joachim Maier, and Yuichi Ikuhara. Lithium Storage in Li4ti5o12 Spinel: The Full Static Picture from Electron Microscopy. *Advanced Materials*, 24(24):3233–3238, 2012.

[7] Zachary Arthur, Hsien-Chieh Chiu, Xia Lu, Ning Chen, Vincent Emond, Karim Zaghib, De-Tong Jiang, and George P.Demopoulos. Spontaneous reaction between an uncharged lithium iron silicate cathode and a LiPF 6 -based electrolyte. *Chemical Communications*, 52(1):190–193, 2016.

[8] Simon Mller, Patrick Pietsch, Ben-Elias Brandt, Paul Baade, Vincent De Andrade, Francesco De Carlo, and Vanessa Wood. Quantification and modeling of mechanical degradation in lithium-ion batteries based on nanoscale imaging. *Nature Communications*, 9(1):2340, June 2018.

[9] A. Van der Ven, G. Ceder, M. Asta, and P. D. Tepesch. First-principles theory of ionic diffusion with nondilute carriers. *Physical Review B*, 64(18):184307, October 2001.

[10] Hsien-chieh Chiu, Nicolas Brodusch, Raynald Gauvin, Abdelbast Guerfi, Karim Zaghib, and George P. Demopoulos. Aqueous Synthesized Nanostructured Li4ti5o12 for High-Performance Lithium Ion Battery Anodes. *Journal of The Electrochemical Society*, 160(5):A3041–A3047, January 2013.

[11] B. J. Inkson. Scanning electron microscopy (sem) and transmission electron microscopy (tem) for materials characterization. In Gerhard Hbschen, Iris Altpeter, Ralf Tschuncky, and Hans-Georg Herrmann, editors, *Materials Characterization Using Nondestructive Evaluation (NDE) Methods*, pages 17–43. Woodhead Publishing, 2016.

[12] Thomas W. Hansen, Jakob B. Wagner, Poul L. Hansen, Sren Dahl, Haldor Topse, and Claus J. H. Jacobsen. Atomic-Resolution in Situ Transmission Electron Microscopy of a Promoter of a Heterogeneous Catalyst. *Science*, 294(5546):1508–1510, November 2001.

[13] Shunsuke Kobayashi, Craig A. J. Fisher, Akihide Kuwabara, Yoshio Ukyo, and Yuichi Ikuhara. Quantitative analysis of Li distributions in battery material Li1-xFePO4 using Fe M2,3-edge and valence electron energy loss spectra. *Microscopy*, 66(4):254–260, August 2017.

[14] RF Egerton. Eels in the electron microscope. *Springer, New York p*, 226, 1986.

[15] Takeshi Sunaoshi, Yoshihisa Orai, Hiroyuki Ito, Takeshi Ogashiwa, Toshihide Agemura, and Mitsuru Konno. 30 kv stem imaging with lattice resolution using a high resolution cold fe-sem. 2012.

[16] W. Kohn and L. J. Sham. Self-Consistent Equations Including Exchange and Correlation Effects. *Physical Review*, 140(4A):A1133–A1138, 1965.

[17] K. Schwarz, P. Blaha, and G. K. H. Madsen. Electronic structure calculations of solids using the WIEN2k package for material sciences. *Computer Physics Communications*, 147(1):71–76, 2002.

[18] The Elk FP-LAPW Code.

[19] Andris Gulans, Stefan Kontur, Christian Meisenbichler, Dmitrii Nabok, Pasquale Pavone, Santiago Rigamonti, Stephan Sagmeister, Ute Werner, and Claudia Draxl. exciting: a full-potential all-electron package implementing density-functional theory and many-body perturbation theory. *Journal of Physics: Condensed Matter*, 26(36):363202, 2014.

[20] Jrgen Hafner. Ab-initio simulations of materials using VASP: Density-functional theory and beyond. *Journal of Computational Chemistry*, 29(13):2044–2078, 2009.

[21] V. Mauchamp, F. Boucher, G. Ouvrard, and P. Moreau. Ab initio simulation of the electron energy-loss near-edge structures at the lik edge in li, li2o, and limn2o4. *Physical Review B*, 74(11):115106, 2006. WOS:000240872300038.

[22] V. Mauchamp, P. Moreau, G. Ouvrard, and F. Boucher. Local field effects at Li K edges in electron energy-loss spectra of Li, ${\mathrm{Li}}_{2}\mathrm{O}$ and LiF. *Physical Review B*, 77(4):045117, January 2008.

[23] Joseph I. Goldstein, Dale E. Newbury, Patrick Echlin, David C. Joy, Charles E. Lyman, Eric Lifshin, Linda Sawyer, and Joseph R. Michael. *Scanning Electron Microscopy and X-ray Microanalysis*. Springer, Boston, MA, 2003.

[24] Michael J. Rust, Mark Bates, and Xiaowei Zhuang. Sub-diffraction-limit imaging by stochastic optical reconstruction microscopy (storm). *Nature Methods*, 3(10):793–796, 2006.

[25] Eugene Hecht. Optics. *Addison Wesley*, 997:213–214, 1998.

[26] Alfredo M. Morales and Charles M. Lieber. A Laser Ablation Method for the Synthesis of Crystalline Semiconductor Nanowires. *Science*, 279(5348):208–211, 1998.

[27] David B. Williams and C. Barry Carter. *Transmission electron microscopy: a textbook for materials science*. Springer, New York, 2nd ed edition, 2008.

[28] Ludwig Reimer. Electron optics of a scanning electron microscope. In *Scanning Electron Microscopy*, Springer Series in Optical Sciences, pages 13–56. Springer, Berlin, Heidelberg, 1998.

[29] Maria Varela, Jaume Gazquez, and Stephen J. Pennycook. Stem-eels imaging of complex oxides and interfaces. *MRS Bulletin*, 37(1):29–35, 2012.

[30] Christian Colliex. An illustrated review of various factors governing the high spatial resolution capabilities in eels microanalysis. *Ultramicroscopy*, 18(1):131–150, 1985.

[31] T. Malis, S. C. Cheng, and R. F. Egerton. Eels log-ratio technique for specimen-thickness measurement in the tem. *Journal of Electron Microscopy Technique*, 8(2):193–200, 1988.

[32] Jaysen Nelayah, Mathieu Kociak, Odile Stphan, F. Javier Garca de Abajo, Marcel Tenc, Luc Henrard, Dario Taverna, Isabel Pastoriza-Santos, Luis M. Liz-Marzn, and Christian Colliex. Mapping surface plasmons on a single metallic nanoparticle. *Nature Physics*, 3(5):348–353, 2007.

[33] Ann-Lenaig Hamon, Jo Verbeeck, Dominique Schryvers, Jan Benedikt, and Richard M. C. M. v d Sanden. Elnes study of carbon k-edge spectra of plasma deposited carbon films. *Journal of Materials Chemistry*, 14(13):2030–2035, 2004.

[34] G. Torrisi, A. Di Mauro, M. Scuderi, G. Nicotra, and G. Impellizzeri. Atomic layer deposition of ZnO/TiO 2 multilayers: towards the understanding of Ti-doping in ZnO thin films. *RSC Advances*, 6(91):88886–88895, 2016.

[35] Helmut Kohl and Ludwig Reimer. *Transmission Electron Microscopy: Physics of Image Formation*. Number 36 in Springer Series in Optical Sciences. Springer, New York, NY, 2008.

[36] David J Griffiths. *Introduction to electrodynamics*. 2013. OCLC: 794711764.

[37] Jordan A. Hachtel, Andrew R. Lupini, and Juan Carlos Idrobo. Exploring the capabilities of monochromated electron energy loss spectroscopy in the infrared regime. *Scientific Reports*, 8(1):5637, April 2018.

[38] Kisuk Kang and Gerbrand Ceder. Factors that affect Li mobility in layered lithium transition metal oxides. *Physical Review B*, 74(9):094105, September 2006.

[39] H. Tenailleau and J. M. Martin. A new background subtraction for low-energy eels core edges. *Journal of Microscopy*, 166(3):297–306, 1992.

[40] J. Verbeeck and S. Van Aert. Model based quantification of EELS spectra. *Ultramicroscopy*, 101(2):207–224, 2004.

[41] R. F. Egerton. Inelastic scattering of 80 keV electrons in amorphous carbon. *The Philosophical Magazine: A Journal of Theoretical Experimental and Applied Physics*, 31(1):199–215, 1975.

[42] T. Riedl, T. Gemming, and K. Wetzig. Extraction of EELS white-line intensities of manganese compounds: Methods, accuracy, and valence sensitivity. *Ultramicroscopy*, 106(4):284–291, March 2006.

[43] A. Gloter, A. Douiri, M. Tenc, and C. Colliex. Improving energy resolution of eels spectra: an alternative to the monochromator solution. *Ultramicroscopy*, 96(3):385–400, 2003.

[44] J. E. Krist. Deconvolution of hubble space telescope images using simulated point spread functions. *Astronomical Data Analysis Software and Systems I, A.S.P. Conference Series*, 25:226–227, 1992.

[45] Frank de Groot. High-resolution x-ray emission and x-ray absorption spectroscopy, 2001.

[46] Ian MacLaren, Kirsty J. Annand, Colin Black, and Alan J. Craven. EELS at very high energy losses. *Microscopy*, 67(suppl_1):i78–i85, 2018.

[47] Codes - NOMAD, 2018.

[48] David S Sholl and Janice A Steckel. *Density functional theory: a practical introduction.* Wiley, Hoboken, N.J., 2009. OCLC: 441874984.

[49] E. K. U. Gross and K. Burke. *Time-Dependent Density Functional Theory.* Lecture Notes in Physics. Springer, Berlin, Heidelberg, 2006.

[50] G. Grff, H. Kalinowsky, and J. Traut. A direct determination of the proton electron mass ratio. *Zeitschrift fr Physik A Atoms and Nuclei*, 297(1):35–39, 1980.

[51] P. Hohenberg and W. Kohn. Inhomogeneous electron gas. *Physical Review*, 136(3B):B864–B871, 1964.

[52] R G Parr. Density Functional Theory. *Annual Review of Physical Chemistry*, 34(1):631–656, 1983.

[53] Jianmin Tao, John P. Perdew, Viktor N. Staroverov, and Gustavo E. Scuseria. Climbing the Density Functional Ladder: Nonempirical Meta–Generalized Gradient Approximation Designed for Molecules and Solids. *Physical Review Letters*, 91(14):146401, 2003.

[54] John P. Perdew, Kieron Burke, and Yue Wang. Generalized gradient approximation for the exchange-correlation hole of a many-electron system. *Physical Review B*, 54(23):16533–16539, 1996.

[55] Axel D. Becke and Erin R. Johnson. A simple effective potential for exchange. *The Journal of Chemical Physics*, 124(22):221101, 2006.

[56] M. J. Frisch et al. Gaussian16 Revision B.01, 2016. Gaussian Inc. Wallingford CT.

[57] Stephan Mohr, Marc Eixarch, Maximilian Amsler, Mervi J. Mantsinen, and Luigi Genovese. Linear scaling DFT calculations for large tungsten systems using an optimized local basis. *Nuclear Materials and Energy*, 15:64–70, May 2018.

[58] David J. Griffiths. *Introduction to quantum mechanics*. Pearson Prentice Hall, Upper Saddle River, NJ, 2005.

[59] Paolo Giannozzi and Baroni. QUANTUM ESPRESSO: a modular and open-source software project for quantum simulations of materials. *Journal of Physics: Condensed Matter*, 21(39):395502, 2009.

[60] David J. Singh and Lars Nordstrm. *Planewaves, Pseudopotentials, and the LAPW Method*. Springer, New York, NY, UNITED STATES, 2006.

[61] Richard F. W. Bader. Atoms in Molecules. In *Encyclopedia of Computational Chemistry*. American Cancer Society, 2002.

[62] Richard F. W. Bader. A quantum theory of molecular structure and its applications. *Chemical Reviews*, 91(5):893–928, 1991.

[63] A. Otero-de-la Roza, Erin R. Johnson, and Vctor Luaa. Critic2: A program for real-space analysis of quantum chemical interactions in solids. *Computer Physics Communications*, 185(3):1007–1018, 2014.

[64] Malte Fugel, Jens Beckmann, Dylan Jayatilaka, Gerald V. Gibbs, and Simon Grabowsky. A Variety of Bond Analysis Methods, One Answer? An Investigation of the ElementOxygen Bond of Hydroxides HnXOH. *Chemistry A European Journal*, 24(23):6248–6261, 2018.

[65] Claudia Ambrosch-Draxl and Jorge O. Sofo. Linear optical properties of solids within the full-potential linearized augmented planewave method. *Computer Physics Communications*, 175(1):1–14, 2006.

[66] A. L. Ankudinov, B. Ravel, J. J. Rehr, and S. D. Conradson. Real-space multiple-scattering calculation and interpretation of x-ray-absorption near-edge structure. *Physical Review B*, 58(12):7565–7576, 1998.

[67] C. Hebert. Practical aspects of running the WIEN2k code for electron spectroscopy. *Micron*, 38(1):12–28, 2007. WOS:000241994700002.

[68] E. E. Salpeter and H. A. Bethe. A Relativistic Equation for Bound-State Problems. *Physical Review*, 84(6):1232–1242, 1951.

[69] Stephan Sagmeister and Claudia Ambrosch-Draxl. Time-dependent density functional theory versus BetheSalpeter equation: an all-electron study. *Physical Chemistry Chemical Physics*, 11(22):4451–4457, 2009.

[70] P. A. Lee and G. Beni. New method for the calculation of atomic phase shifts: Application to extended x-ray absorption fine structure (EXAFS) in molecules and crystals. *Physical Review B*, 15(6):2862–2883, 1977.

[71] Vincent Mauchamp, Michel Jaouen, and Peter Schattschneider. Core-hole effect in the one-particle approximation revisited from density functional theory. *Physical Review B*, 79(23):235106, 2009.

[72] J. Luitz, M. Maier, C. Hbert, P. Schattschneider, P. Blaha, K. Schwarz, and B. Jouffrey.

Partial core hole screening in the Cu L3 edge. *The European Physical Journal B*, 21(3):363–367, 2001.

[73] C. Hebert, J. Luitz, and P. Schattschneider. Improvement of energy loss near edge structure calculation using Wien2k. *Micron*, 34(3-5):219–225, 2003. WOS:000184846600012.

[74] J. C. Slater. Energy Band Calculations by the Augmented Plane Wave Method**The research reported in this paper has been assisted by the National Science Foundation and the Office of Naval Research, as well as by the Army, Navy, and Air Force. *Advances in Quantum Chemistry*, 1:35–58, January 1964.

[75] R. Brydson, J. Bruley, and J. M. Thomas. Further evidence for core-hole effects in the near-edge structures of light-element K-edges. *Chemical Physics Letters*, 149(4):343–347, 1988.

[76] T. P. Hardcastle, C. R. Seabourne, D. M. Kepaptsoglou, T. Susi, R. J. Nicholls, R. M. D. Brydson, A. J. Scott, and Q. M. Ramasse. Robust theoretical modelling of core ionisation edges for quantitative electron energy loss spectroscopy of B- and N-doped graphene. *Journal of Physics: Condensed Matter*, 29(22):225303, 2017.

[77] E. W. Tait, L. E. Ratcliff, M. C. Payne, P. D. Haynes, and N. D. M. Hine. Simulation of electron energy loss spectra of nanomaterials with linear-scaling density functional theory. *Journal of Physics: Condensed Matter*, 28(19):195202, 2016.

[78] P. Jegadeesan, S. Amirthapandian, Gurpreet Kaur, Sharat Chandra, and B. K. Panigrahi. Characterization of MO bonds in Y2ti2o7 and Y2tio5 with EELS. *physica status solidi (b)*, 252(1):206–211, 2015.

[79] Damien Magne, Vincent Mauchamp, Stphane Clrier, Patrick Chartier, and Thierry Cabioc'h. Site-projected electronic structure of two-dimensional Ti 3 C 2 MXene: the role of the surface functionalization groups. *Physical Chemistry Chemical Physics*, 18(45):30946–30953, 2016.

[80] P. Agrawal, J. Guo, P. Yu, C. Hbert, D. Passerone, R. Erni, and M. D. Rossell. Strain-driven oxygen deficiency in multiferroic ${\mathrm{SrMnO}}_{3}$ thin films. *Physical Review B*, 94(10):104101, September 2016.

[81] Kota Tomita, Tomohiro Miyata, Weine Olovsson, and Teruyasu Mizoguchi. Strong excitonic interactions in the oxygen K-edge of perovskite oxides. *Ultramicroscopy*, 178:105–111, July 2017.

[82] Nicholas L. McDougall, Rebecca J. Nicholls, Jim G. Partridge, and Dougal G. McCulloch. The Near Edge Structure of Hexagonal Boron Nitride. *Microscopy and Microanalysis*, 20(4):1053–1059, August 2014.

[83] Tomohiro Miyata and Teruyasu Mizoguchi. Fabrication of thin TEM sample of ionic liquid for high-resolution ELNES measurements. *Ultramicroscopy*, 178:81–87, July 2017.

[84] Robert F. Klie, Haibin Su, Yimei Zhu, James W. Davenport, Juan-Carlos Idrobo, Nigel D. Browning, and Peter D. Nellist. Measuring the hole-state anisotropy in ${\mathrm{MgB}}_{2}$ by electron energy-loss spectroscopy. *Physical Review B*, 67(14):144508, April 2003.

[85] Stefan Nufer, Thomas Gemming, Christian Elssser, Sibylle Kstlmeier, and Manfred Rhle. Core-hole effect in the ELNES of -Al2o3: experiment and theory. *Ultramicroscopy*, 86(3):339–342, February 2001.

[86] Shang-Peng Gao, Chris J. Pickard, Alexander Perlov, and Victor Milman. Core-level spectroscopy calculation and the plane wave pseudopotential method. *Journal of Physics: Condensed Matter*, 21(10):104203, 2009.

[87] Kevin Jorissen. *The ab initio calculation of relativistic electron energy loss spectra*. PhD thesis, University of Antwerp, 2007.

[88] W. Kohn and L. J. Sham. Self-Consistent Equations Including Exchange and Correlation Effects. *Physical Review*, 140(4A):A1133–A1138, 1965.

[89] E. L. Shirley, J. A. Soininen, and J. J. Rehr. Modeling core-hole screening in core-excitation spectroscopies. *Physica Scripta*, 2005(T115):31, 2005.